General-relativistic neutrino-radiation magnetohydrodynamic simulation of seconds-long black hole-neutron star mergers

Kota Hayashi[●],[1] Sho Fujibayashi[●],[2] Kenta Kiuchi[●],[2,1] Koutarou Kyutoku,[3,1,4]
Yuichiro Sekiguchi[5,1] and Masaru Shibata[2,1]

[1]*Center for Gravitational Physics, Yukawa Institute for Theoretical Physics, Kyoto University,
Kyoto 606-8502, Japan*
[2]*Max Planck Institute for Gravitational Physics (Albert Einstein Institute),
Am Mühlenberg 1, Potsdam-Golm 14476, Germany*
[3]*Department of Physics, Kyoto University, Kyoto 606-8502, Japan*
[4]*Interdisciplinary Theoretical and Mathematical Sciences Program (iTHEMS),
RIKEN, Wako, Saitama 351-0198, Japan*
[5]*Department of Physics, Toho University, Funabashi, Chiba 274-8510, Japan*

Seconds-long numerical-relativity simulations for black hole–neutron star mergers are performed for the first time to obtain a self-consistent picture of the merger and post-merger evolution processes. To investigate the case that tidal disruption takes place, we choose the initial mass of the black hole to be 5.4 $M_\odot$ or 8.1 $M_\odot$ with a dimensionless spin of 0.75. The neutron-star mass is fixed to be 1.35 $M_\odot$. We find that after the tidal disruption, dynamical mass ejection takes place over $\lesssim 10$ ms, together with the formation of a massive accretion disk. Subsequently, the magnetic field in the disk is amplified by the magnetic winding and magnetorotational instability, establishing a turbulent state and inducing angular momentum transport. The post-merger mass ejection by the magnetically induced viscous effect sets in at ~ 300–500 ms after the tidal disruption, at which the neutrino luminosity drops below $\sim 10^{51.5}$ erg/s, and continues for several hundred ms. A magnetosphere near the rotational axis of the black hole is developed after the matter and magnetic flux fall into the black hole from the accretion disk, and high-intensity Poynting flux generation sets in at a few hundred ms after the tidal disruption. The intensity of the Poynting flux becomes low after the significant post-merger mass ejection, because the opening angle of the magnetosphere increases. The lifetime of the stage with the strong Poynting flux is 1–2 s, which agrees with the typical duration of short-hard gamma-ray bursts.

I. INTRODUCTION

The era of gravitational-wave astronomy began with the first observation of a binary black hole merger, referred to as GW150914 [1]. To date, ~ 80 binary black hole merger events have been observed by Advanced LIGO and Advanced Virgo [2,3]. In addition to binary black holes, a couple of neutron-star binaries have also been observed. In particular, associated with the first binary neutron star merger event GW170817 [4], a wide variety of the signals of the electromagnetic counterpart were successfully detected [5,6]. This event opened the multimessenger astronomy including gravitational-wave observation.

In addition, gravitational-wave signals from the black hole–neutron star mergers GW200105 and GW200115 were detected in 2020 [7]. These events surely indicate that black hole–neutron star binaries exist in nature. Although no electromagnetic counterpart was detected for these two events, a number of numerical-relativity simulations for the black hole–neutron star mergers have

predicted that tidal disruption of the neutron star and subsequent mass ejection should take place if the parameters of the source (black-hole mass, black-hole spin, and neutron-star compactness) are in appropriate ranges [8,9]. If the remnant black hole is rapidly spinning and surrounded by a magnetized massive torus, an ultrarelativistic jet is likely to drive a short-hard gamma-ray burst [10–12]. In the presence of mass ejection, r-process nucleosynthesis inevitably proceeds [10,13], and subsequently the ejecta should shine with a high luminosity associated with the thermal energy generated by the radioactive decay of neutron-rich heavy elements [14,15]. Since the sensitivity of gravitational-wave detectors and electromagnetic telescopes is improving every year, it is quite natural to expect that electromagnetic counterparts of black hole–neutron star mergers will be observed in the near future if the distance to the source is within several hundred Mpc, and thus black hole–neutron star mergers are among the most promising sources for multimessenger astronomy. In this situation, theoretical studies to elucidate the entire process

023008-1

from tidal disruption to post-merger evolution are required to predict observable signals.

In the last 15 years, a variety of numerical-relativity simulations have been performed for black hole–neutron star mergers [16–50], improving the input physics and grid resolutions, and the processes of tidal disruption and subsequent accretion disk formation, merger remnants, dynamical mass ejection, gravitational waves, and neutrino emissivity have been extensively studied. However, all of this work has focused primarily on the inspiral to early merger stages, and hence the long-term (seconds-long) post-merger process has not been explored in these simulations. To compensate for this drawback, many numerical simulations (viscous hydrodynamics or magnetohydrodynamics simulations) have also been performed to explore the long-term evolution of the accretion disks (or tori) around a black hole [51–66], and have clarified the post-merger mass ejection mechanisms and properties of the post-merger ejecta. These works reported that the post-merger mass ejection is driven primarily by a viscous hydrodynamics effect induced by the magnetohydrodynamics turbulence in the accretion disks and by a Lorentz force associated with the amplified magnetic fields. Although these works are important for understanding the post-merger mass ejection mechanisms, the initial conditions for the simulations were *ad hoc* or some important physical inputs were absent, and hence the conclusive quantitative details such as quantitative properties of the post-merger ejecta have not been fully understood yet.

In order to acquire a full understanding of black hole–neutron star mergers and associated mass ejection processes, we need to perform a self-consistent simulation starting from the inspiral stage and through to the post-merger stage. Specifically, the post-merger evolution has to be followed at least for a few seconds, because the post-merger mass ejection takes place over a time scale of $\gtrsim 1$ s. Furthermore, to explore the generation mechanism of short-hard gamma-ray bursts, a simulation with a duration of $\gtrsim 1$ s is needed because their typical duration is ~ 1 s, with the longest duration being ~ 2 s [11,12]. Keeping these time scales in mind, in this paper we tackle this problem by performing general-relativistic neutrino-radiation magnetohydrodynamics simulations of black hole–neutron star mergers for ≈ 1–2 s. Here we emphasize that both the neutrino radiation transfer and magnetohydrodynamics effects are necessary elements for determining the evolution of the merger remnant. In this long-term simulation with the relevant physics, the magnetohydrodynamics turbulence and associated angular-momentum transport in the accretion disk are naturally taken into account, and furthermore a black-hole magnetosphere in the vicinity of the rotation axis of the remnant spinning black hole—which could be suitable for generating a short-hard gamma-ray burst—also naturally emerges.

This paper is organized as follows. In Sec. II we briefly summarize the method and initial setup for the numerical simulation. In Sec. III we present the numerical results, focusing on the entire evolution process, mass ejection mechanisms, and collimated electromagnetic outflow developed near the rotation axis of the black hole. Finally, we conclude this work in Sec. IV. Throughout the paper we adopt geometrical units in which $G = c = 1$, where G and c are the gravitational constant and speed of light, respectively.

II. METHODS

Our numerical implementation for the present simulations is the same as that in Ref. [41] except for the ideal magnetohydrodynamics part, for which we implement the scheme used in Ref. [39]. Specifically, we solve Einstein's equation using a puncture-Baumgarte-Shapiro-Shibata-Nakamura (BSSN) formalism [67–71], incorporating a Z4c-type constraint-propagation prescription [38,72]. In this work the original version of the BSSN formalism [67] is employed. A fourth-order finite-differencing scheme is applied to discretize the gravitational-field equation. Magnetohydrodynamics equations are solved in a high-resolution shock-capturing scheme [73–75], together with a second-order constrained-transport scheme [76] and Balsara's flux-preserving mesh refinement scheme [77]. Neutrino transfer is handled using a leakage-based scheme [78], together with a truncated moment formalism using a closure relation for the free-streaming component [79,80]. Neutrino heating and absorption on free nucleons are incorporated using an updated numerical procedure [81]. We do not take the neutrino pair annihilation effect into account in this paper.

The simulation is performed using a fixed-mesh refinement (FMR) algorithm with the equatorial symmetry imposed at $z = 0$. The ith refinement level covers a half-cubic region of $[-L_i : L_i] \times [-L_i : L_i] \times [0 : L_i]$, where $L_i = N \Delta x_i$ and Δx_i is the grid spacing for the ith level. The grid spacing for each level is determined by $\Delta x_i = 2 \Delta x_{i+1}$ ($i = 1, 2, \ldots, i_{\max} - 1$), with $\Delta x_{i_{\max}} = 400$ m for low-resolution runs and $\Delta x_{i_{\max}} = 270$ m for high-resolution runs. $i_{\max}$ is chosen to be 9 or 10. The values of N are 170 or 192 for low-resolution runs and 234 or 282 for high-resolution runs, respectively (cf. Table I).

During the merger stage, the black hole is kicked mainly by the backreaction of the dynamical mass ejection, and the resulting velocity is $v_{\rm kick} = 200$–400 km/s (which is estimated by $m_{\rm ej} v_{\rm ej} / M_{\rm BH}$, where $m_{\rm ej}$ is the dynamical ejecta mass, $v_{\rm ej}(\sim 0.2c)$ is its absolute average velocity, and $M_{\rm BH}$ is the remnant black hole mass) in our present setting. Thus, the black hole moves toward a refinement boundary of the finest FMR level with time and eventually escapes from the highest-resolution level in the absence of any prescription. To keep the black hole in the highest-resolution level,

TABLE I. Key parameters and quantities for the initial conditions together with the parameters of the grid setup for our numerical simulations. $M_{\mathrm{BH,0}}$: the initial black-hole mass; $b_{0,\max}$: the initial maximum magnetic-field strength; Ω_0: the initial orbital angular velocity; $M_{\mathrm{ADM,0}}$: the initial ADM mass; $\Delta x_{i_{\max}}$: the grid spacing for the finest refinement level; L_1: the location of the outer boundaries along each axis; and the values of N and $i_{\max}$. For all models, the neutron-star mass is 1.35 $M_\odot$ and the initial dimensionless black-hole spin is 0.75. Note that $M_{\mathrm{ADM,0}}$ is $\sim 1\%$ smaller than $m_0 = (6.75$ and $9.45\ M_\odot$ for $Q = 4$ and 6) because of the presence of the gravitational binding energy.

Model name	$M_{\mathrm{BH,0}}\ [M_\odot]$	$b_{0,\max}\ [\mathrm{G}]$	$m_0\Omega_0$	$M_{\mathrm{ADM,0}}\ [M_\odot]$	$\Delta x_{i_{\max}}\ [\mathrm{m}]$	$L_1\ [\mathrm{km}]$	N	$i_{\max}$
Q4B5H	5.400	5×10^{16}	0.056	6.679	270	1.62×10^4	234	9
Q4B5L	5.400	5×10^{16}	0.056	6.679	400	1.74×10^4	170	9
Q4B3L	5.400	3×10^{16}	0.056	6.679	400	1.74×10^4	170	9
Q6B5H	8.100	5×10^{16}	0.064	9.368	270	3.90×10^4	282	10
Q6B5L	8.100	5×10^{16}	0.064	9.368	400	3.97×10^4	194	10
Q6B3H	8.100	3×10^{16}	0.064	9.368	270	3.90×10^4	282	10
Q6B3L	8.100	3×10^{16}	0.064	9.368	400	3.97×10^4	194	10

we control the shift vector by modifying the evolution equation in the following way:

$$\partial_t \beta^i = \frac{3}{4}\tilde{\gamma}^{ij}(F_j + \partial_t F_j \Delta t) + \frac{v_{\mathrm{BH}}^i}{T_{\mathrm{relax}}}$$

$$\text{for } T_{\mathrm{sta}} < t < T_{\mathrm{sta}} + T_{\mathrm{relax}}, \qquad (1)$$

$$\partial_t \beta^i = \frac{3}{4}\tilde{\gamma}^{ij}(F_j + \partial_t F_j \Delta t)$$

$$\text{for other cases}, \qquad (2)$$

where β^i is the shift vector, $\tilde{\gamma}_{ij}$ is the conformal three-metric, $F_i = \delta^{jk}\partial_j \tilde{\gamma}_{ki}$ is the auxiliary variable in the original version of the BSSN formalism, Δt is the time-step interval, and v_{BH}^i, T_{relax}, and T_{sta} are constants which we determine appropriately based on the numerical result. v_{BH}^i is the coordinate velocity of the black-hole center (the location of the puncture) just before modifying the shift vector, which is of order $10^{-3}c$, as we already mentioned. T_{relax} is the relaxation time, which we choose to be $T_{\mathrm{relax}} = 40$ ms. T_{sta} is the starting time of this prescription, and it is set to be $T_{\mathrm{sta}} \approx 100$–200 ms to satisfy $v_{\mathrm{kick}}(T_{\mathrm{sta}} + T_{\mathrm{relax}}) \lesssim L_{i_{\max}}/2$.

We stop the time evolution of the gravitational field at a certain moment after the ratio of the rest mass of the remnant disk to the black-hole mass drops below 10^{-2}. This prescription is reasonable because the self-gravity of the matter located outside the black hole can be safely neglected and the gravitational field is approximately stationary in such a low-mass disk stage.

For modeling the neutron-star matter, we employ a nuclear-theory-based finite-temperature equation of state (EOS) referred to as DD2 [82] for the high-density range, and a Helmholtz EOS [83] for the low-density range (see the Appendix A for our method of constructing the EOSs and Appendix B for the heating effect due to nuclear reactions). Initial data are given by calculating a quasiequilibrium state of black hole–neutron star binaries in a quasicircular orbit assuming the neutrinoless beta-equilibrium cold state [41]. The initial gravitational mass of

the neutron star is set to be $M_{\mathrm{NS}} = 1.35\ M_\odot$, following Ref. [41]. The circumferential radius of the isolated spherical neutron star of mass 1.3–1.4 $M_\odot$ is ≈ 13.2 km with this EOS, and it satisfies constraints imposed by the observation of gravitational waves for GW170817 [4] and by the x-ray observation by NICER [84].

For the initial black-hole mass, we choose $M_{\mathrm{BH,0}} = 5.4\ M_\odot$ or $8.1\ M_\odot$; the mass ratio of the black hole to the neutron star is $Q := M_{\mathrm{BH,0}}/M_{\mathrm{NS}} = 4$ or 6. The initial dimensionless spin parameter of the black hole is set to be 0.75. With such a spin, tidal disruption of the neutron star with $M_{\mathrm{NS}} = 1.35\ M_\odot$ takes place for a wide range of Q. The initial orbital angular velocity Ω_0 is set to be $m_0\Omega_0 = 0.056$ for $Q = 4$ and 0.064 for $Q = 6$, where m_0 is the sum of the initial black-hole mass and neutron-star mass, i.e., $m_0 = M_{\mathrm{BH,0}} + M_{\mathrm{NS}} = 1.35(Q + 1)\ M_\odot$. In this initial setup, the binary merges after about three orbits. We note that the binary parameter for $Q = 4$ is the same as that employed for the DD2 EOS in our previous paper [41].

We initially superimpose a poloidal magnetic field confined in the neutron star. Following our previous work [39], the poloidal field is given in terms of the vector potential as

$$A_j = \{-(y - y_{\mathrm{NS}})\delta_j{}^x + (x - x_{\mathrm{NS}})\delta_j{}^y\} \times A_b \max(P/P_{\max} - 10^{-3}, 0)^2, \qquad (3)$$

where $(x_{\mathrm{NS}}, y_{\mathrm{NS}})$ is the coordinate position of the neutron-star center (location of the maximum rest-mass density) in the orbital plane, P is the pressure, $P_{\max}$ is the maximum pressure, and $j = x$, y, and z. A_b is a constant and is chosen so that the initial maximum magnetic-field strength $b_{0,\max}$ is 3×10^{16} G or 5×10^{16} G. These values are chosen to obtain a strong magnetic field in the remnant disk formed after tidal disruption of the neutron star on a short time scale after the merger. The strong magnetic field is required to resolve the fastest growing mode of the magnetorotational instability (MRI) [85,86] in the accretion disk with the

limited grid resolution, because its wavelength is proportional to the magnetic-field strength. Although such strong fields are not realistic in orbiting neutron stars, the resulting turbulent state in the accretion disk established by the MRI is not likely to depend strongly on the initial magnetic-field strength.[1] Thus, it would be reasonable to suppose that the resulting strong magnetic field and turbulent state will be established even for the case where we start a simulation from a much weaker magnetic-field strength in the presence of a sufficient grid resolution. We also note that even with $b_{0,\mathrm{max}} = 5 \times 10^{16}$ G, the electromagnetic energy (of order 10^{49} erg) is much smaller than the internal energy and gravitational potential energy (of order 10^{53} erg) of the neutron star. We do not consider the effect of neutrino viscosity on the MRI, as we assume that the magnetic-field strength could be enhanced to be $\gtrsim 10^{14}$ G due to the rapid winding in the main region of the accretion disk (see Sec. III B) even if the early growth of the MRI is suppressed [87,88].

We perform seven simulations, changing the black-hole mass, value of $b_{0,\mathrm{max}}$, and grid resolution. The parameters and quantities for the seven models employed in this study are summarized in Table I. Numerical simulations with the low-resolution setting are always performed for a duration of ≥ 1 s. In particular, for $Q = 4$ models, the low-resolution simulations are performed for $\gtrsim 2$ s. On the other hand, the high-resolution simulations are performed only for $\lesssim 1$ s because such simulations require an extremely high computational cost. However, as we show below, the results for the low-resolution runs are quantitatively similar to those for the corresponding high-resolution runs, and hence we consider that a fair convergence is achieved even with the low-resolution runs. The computational time with the low-resolution setting for 2 s is about 1400 hours using 64 nodes of our Sakura cluster, in which one node has two Intel Xeon Gold 6248 CPUs (one node has 40 cores).

III. RESULTS

A. Overview of the evolution

First, we summarize the entire merger process found in a seconds-long simulation, presenting the result for model Q4B5L for which the system was evolved up to ~ 2.1 s. Figure 1 displays the snapshot for the rest-mass density, absolute value of the magnetic-field strength, electron fraction Y_e, and temperature T, respectively, in the $x - z$ plane. The magnetic-field strength is defined by $b = (b_\mu b^\mu)^{1/2}$, where b^μ is the magnetic field in the frame

comoving with the fluid and the temperature (kT where k is the Boltzmann constant) is shown in units of MeV.

For the present choice of the dimensionless spin parameter for the black hole and the fairly large radius of the neutron star, the neutron star is tidally disrupted by the black hole before the binary reaches the innermost stable circular orbit for both $Q = 4$ and 6. During the tidal disruption process, the neutron-star matter located on the black-hole side falls into the black hole. Specifically, $\sim 80\%$ of the neutron-star matter falls into the black hole on a short time scale of a few ms. On the other hand, the neutron-star matter located distant from the black hole forms a one-armed spiral structure. Due to the subsequent angular-momentum transport inside the spiral arm and the dynamical evolution of the black-hole spacetime resulting from the matter infall into the black hole, a part of the matter in the outer part of the spiral arm gains specific energy and angular momentum. The matter that gains sufficient specific energy eventually becomes dynamical ejecta, while the other part in the spiral arm which is bound to the remnant black hole forms an accretion disk. The time scale of this stage is $\lesssim 10$ ms (see the first row of Fig. 1 for the resulting state). All of these processes have been studied in a number of previous numerical-relativity works, and our present result on the tidal disruption and disk formation processes is essentially the same as the previous findings.

The mass (M_{BH}) and dimensionless spin parameter (χ_{BH}) of the remnant black holes evaluated at $t = 100$ ms are summarized in Table II. Irrespective of the runs, the black-hole mass and dimensionless spin are increased by $\approx 1.05\ M_\odot$ and ~ 0.1, respectively, due to the matter infall. The black-hole mass is $\sim 0.3\ M_\odot$ smaller than the initial Arnowitt-Deser-Misner (ADM) mass. The reason for this is that a part of the neutron-star matter forms an accretion disk and ejecta, and gravitational waves and neutrinos carry away the energy (see Tables I and II) in the inspiral and early merger stages.

We also list the total gravitational-wave and neutrino energy emitted before $t = 100$ ms, E_{GW} and E_ν, and the rest mass of the matter located outside the apparent horizon at $t = 100$ ms, $M_{>\mathrm{AH},0.1}$, in Table II. By comparing M_{BH} and $M_{\mathrm{ADM},0} - E_{\mathrm{GW}} - E_\nu - M_{>\mathrm{AH},0.1}$, we can assess how good (or bad) the energy conservation is satisfied in our simulation. It is found that for $Q = 4$, the energy conservation is satisfied with about 0.1% and 1.1% error for high- and low-resolution runs of the $Q = 4$ model, and with $\ll 0.1\%$ and about 0.1% error for high- and low-resolution runs of the $Q = 6$ model, respectively. The reason that the accuracy depends strongly on the grid resolution for $Q = 4$ (i.e., for the smaller black-hole mass) is that the accuracy for resolving the black hole depends strongly on it. This is found by taking a look at the value of the black-hole mass for $Q = 4$: for the low-resolution runs, the black-hole mass is underestimated. However, the error of $\lesssim 1\%$ at $t = 100$ ms is still at an acceptable level, indicating the reliability of the numerical results.
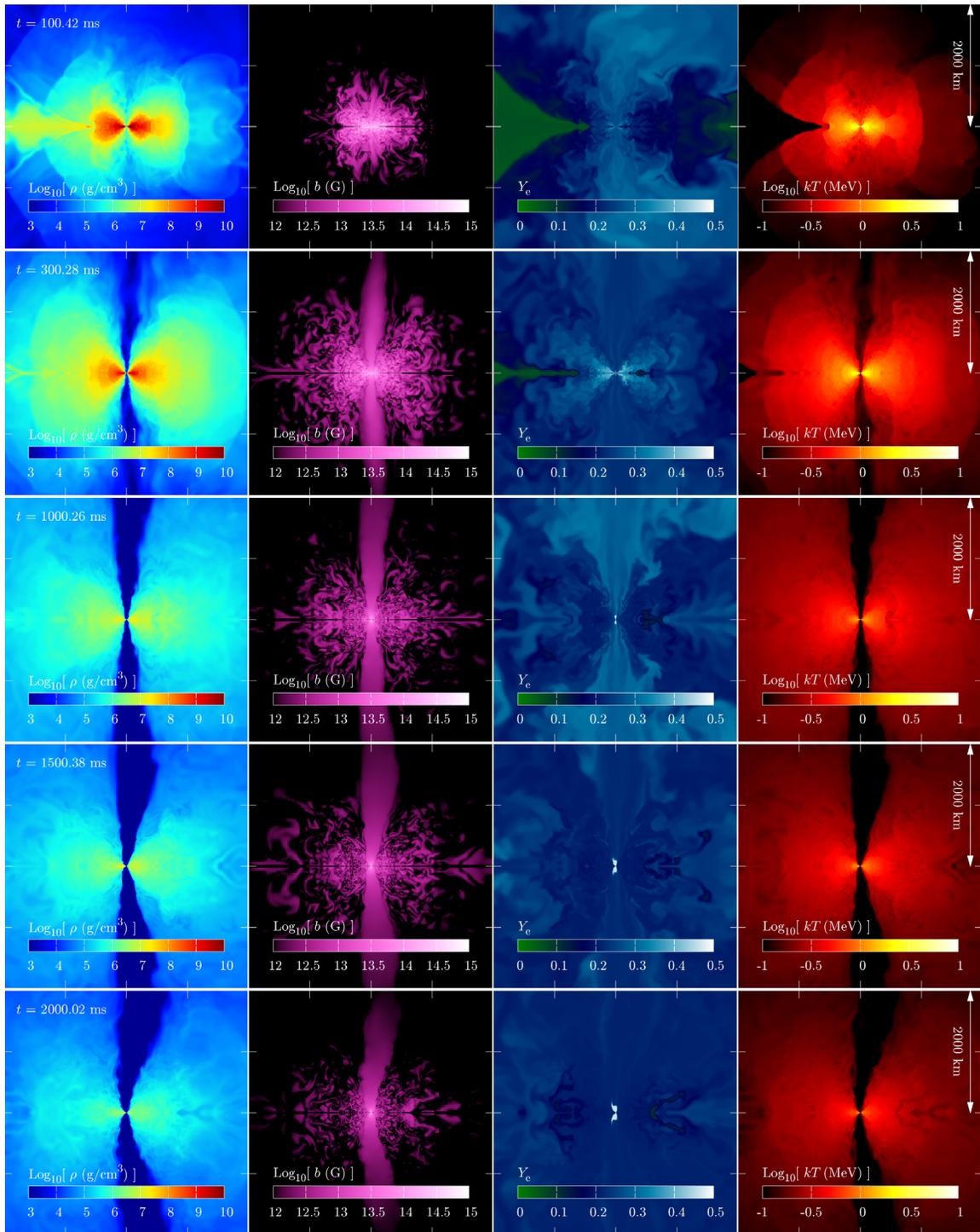
---

[1]That is, we implicitly assume that the magnetic-field strength would be increased by the MRI and a turbulent state would be eventually established even if we started a simulation from low magnetic-field strengths (as is often done in this research field). This is just an assumption, and confirming this by better-resolved simulations remains as an issue for the future.

FIG. 1.   Snapshot of the rest-mass density ρ (g/cm^3), magnetic-field strength $b = \sqrt{b^\mu b_\mu}$ (G), electron fraction Y_e, and temperature T (kT in units of MeV) in the x-z plane with [-2000 km : 2000 km] for both x and z at $t \approx 0.1$, 0.3, 1.0, 1.5, and 2.0 s for model Q4B5L. Note that the green region in Y_e found on the left side in the first and second rows shows the dynamical ejecta and fall-back matter. See also the animation at [89].

After the spiral arm winds around the black hole, a compact accretion disk is formed. The orbital period at the innermost region of the accretion disk is 1–2 ms. During the tidal disruption process, the neutron-star matter which eventually forms an accretion disk experiences a strong differential rotation stage in the spiral arm, and then a toroidal magnetic field develops from the initially poloidal magnetic field by winding. After the formation of the

TABLE II.   Mass M_{BH} and dimensionless spin parameter χ_{BH} of the remnant black hole evaluated at $t = 100$ ms together with the gravitational-wave and neutrino energy emitted before $t = 100$ ms, E_{GW} and E_ν, and the rest mass of the matter located outside the black hole at $t = 100$ ms, $M_{>\mathrm{AH},0.1}$. All quantities related to the mass or energy are described in units of $M_\odot$.

Model	M_{BH}	χ_{BH}	E_{GW}	E_ν	$M_{>\mathrm{AH},0.1}$
Q4B5H	6.466	0.856	0.069	0.008	0.129
Q4B5L	6.400	0.838	0.066	0.008	0.135
Q4B3L	6.396	0.838	0.066	0.008	0.138
Q6B5H	9.145	0.837	0.117	0.007	0.097
Q6B5L	9.138	0.832	0.112	0.007	0.104
Q6B3H	9.145	0.838	0.117	0.007	0.097
Q6B3L	9.136	0.833	0.112	0.007	0.106

accretion disk, the winding continues to enhance the toroidal magnetic-field strength, in particular in the innermost region of the accretion disk. After a sufficient amplification of the magnetic-field strength, an outward expansion of the matter is driven toward the polar direction due to the enhanced magnetic pressure, and as a result poloidal fields for which the strength is comparable to that of the toroidal fields are also generated. With these strong magnetic fields, the wavelength for the fastest growing mode of the MRI becomes ~10 km and can be numerically resolved (see Appendix C). Then, a turbulent state associated with the MRI is developed, and eventually an MRI dynamo is activated in the accretion disk. This can also be observed from a spacetime diagram of the toroidal-field strength. In Fig. 2 we plot the average value of the toroidal field as a function of time and polar angle $\theta = \tan^{-1}(\sqrt{x^2 + y^2}/z)$ for models Q4B5L and Q4B5H. Here, x, y, and z are defined with respect to the black-hole center. The toroidal field is defined by $b_{\bar{\varphi}} = (x b_y - y b_x)/\sqrt{x^2 + y^2}$. The average is performed with respect to the azimuthal angle $\varphi = \tan^{-1}(y/x)$ at the selected radius of $r := \sqrt{x^2 + y^2 + z^2} \approx 50$ km. From Fig. 2, we find the so-called butterfly structure [90] irrespective of the grid resolution: the polarity of the toroidal magnetic field is reversed due to the turbulent motion in a periodic manner with a period of ~20 local orbital periods (≈ 2.5 ms).[2] It is also found that strong magnetic-field regions move from the accretion disk to the polar region in the early stage, producing a global magnetic-field structure (see also the magnetic-field strength in the second row of Fig. 1).

During this turbulent stage, the angular momentum is transported from the inner to the outer region of the accretion disk due to the effective viscosity induced by the turbulence. In addition to this effective viscous process, magnetohydrodynamics effects such as the magneto-centrifugal effect [91] which results from a global magnetic field could play an important role in expelling the matter from the central region. Due to these effects, the matter near the innermost stable circular orbit loses its angular momentum and falls into the black hole, while the matter in the outer part of the disk receives angular momentum and gradually expands. As a result, the rest-mass density and the temperature in the disk decrease in the viscous time scale of order 100 ms to 1 s (see the third to fifth rows of Fig. 1).

In addition to the disk expansion toward the equatorial direction, the matter expands toward the direction perpendicular to the orbital plane (see Fig. 1). Our interpretation of this expansion is that the magnetic tower effect plays a role: during the evolution of the accretion disk, the toroidal magnetic-field strength is enhanced by the MRI and winding. As a result, the magnetic pressure is enhanced to be high enough for the accretion disk to expand toward the direction perpendicular to the orbital plane (and thus the disk becomes a torus), while the serious baryon contamination in the vicinity of the rotational axis is prevented by the centrifugal force of the matter. This effect produces a funnel structure around the rotational axis (see the second to fifth rows of Fig. 1).[3]

In spite of the enhanced magnetic-field strength, we do not find appreciable early-post-merger mass ejection (which might occur within 100–200 ms after the onset of the merger) associated with this enhancement. The absence of a clear early post-merger mass ejection agrees with some of the results found in Ref. [59] in which the initial magnetic-field profile was chosen to be toroidal or weakly poloidal. An early post-merger mass ejection was only found in several previous magnetohydrodynamics studies [56,57,59,60] in which a strong poloidal magnetic field was given. In our simulations, the magnetic-field profile in the early stage of the post-merger evolution is primarily toroidal. Thus, we consider that the early post-merger mass ejection takes place only for the case that a strong poloidal field is present in the disk at the formation of the remnant disk, although our result indicates that such strong poloidal fields are not likely to form soon after the merger of black hole–neutron star binaries.

Both the magnetohydrodynamics effect and neutrino cooling play important roles for the evolution of the accretion disk [51]. In the early stage of the accretion disk, the maximum density is $\gtrsim 10^{12}$ g/cm^3 and the maximum temperature is several MeV. In addition to the

---

[2]After the post-merger mass ejection sets in at $t \sim 400$ ms (cf. Sec. III B), the periodic butterfly diagram is not observed. However, it is still seen that the polarity of the magnetic field changes with time due to the presence of the turbulent motion. The decrease of the toroidal magnetic-field strength is due to the disk expansion.

[3]In the late stage with $t \gtrsim 1.5$ s, the funnel has an asymmetric structure. This is caused by the fallback of the matter in the tidal tail that is formed predominantly for the negative-x direction at tidal disruption. This fallback also lowers the electron fraction near the black hole in the late phase.
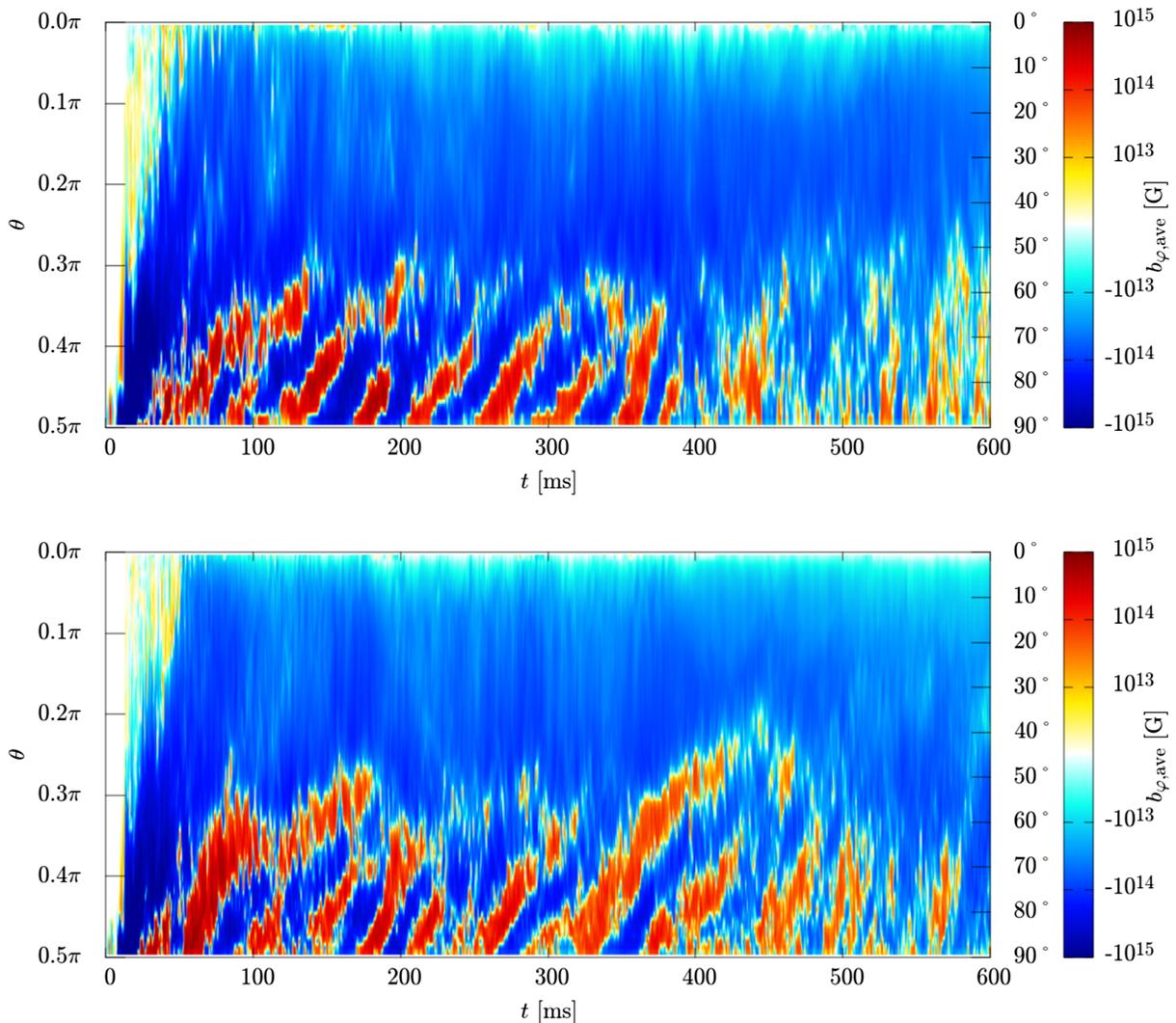
FIG. 2.   Profile of the average toroidal magnetic field along the polar direction (θ) at $r \approx 50$ km as a function of time for models Q4B5L (top panel) and Q4B5H (bottom panel).

high density and high temperature, the disk is massive with a mass $\gtrsim 0.1 \, M_\odot$ in the early stage. In such a stage, the neutrino luminosity becomes higher than 10^{53} erg/s which is comparable to or higher than the viscous heating rate for a compact disk with a high viscous parameter [61]. During the stage when the neutrino luminosity is as high as the rate of the viscous heating (and the shock heating associated with the magnetohydrodynamical activity in the present context), the matter in the accretion disk is not affected significantly by the heating effect, although the accretion disk gradually expands due to the viscous/magnetohydrodynamics angular-momentum transport and magnetic pressure resulting from the enhanced magnetic-field strength. However, with the expansion, the density and temperature of the accretion disk decrease, and consequently the neutrino luminosity sharply decreases because the neutrino emissivity is approximately proportional to T^6 [92]. As the neutrino luminosity drops below the heating rate due to the

viscous and magnetohydrodynamics activities, neutrinos cannot efficiently carry away the thermal energy from the accretion disk and the thermal energy generated by the viscous/magnetohydrodynamics effect influences the evolution of the accretion disk. Specifically, convective motion of the matter in the innermost region of the disk, in which the viscous heating and shock heating are most efficient, is excited and blobs of the matter heated in the vicinity of the black hole are moved toward the outer region of the disk along the surface of the disk.[4] As a result, the matter in the outer part of the disk obtains thermal energy and the heated matter eventually becomes unbound from the system to be the post-merger ejecta (cf. the second and third rows of

---

[4]See the following animations for the entropy per baryon (s/k) and convective activity: https://www2.yukawa.kyoto-u.ac.jp/~kota.hayashi/Q4B5L-2000a.mp4; https://www2.yukawa.kyoto-u.ac.jp/~kota.hayashi/Q4B5L_sent.mp4.

Fig. 1). This mechanism is the same as that found in previous viscous hydrodynamics simulations [51–53,61] (see also Ref. [93]). This post-merger mass ejection continues from 0.2–0.3 s to ∼1 s after the merger (i.e., after the formation of the accretion disk). We note that, in addition to this convective effect, purely magnetohydro-dynamical effects such as the magneto-centrifugal effect [91] could also play a role for the mass ejection.

In parallel with the accretion-disk evolution, a magnetosphere is developed in the low-density region near the rotational axis (see Fig. 1). For the merger of black hole–neutron star binaries that experience tidal disruption, such a low-density region naturally develops because the matter is primarily ejected toward the equatorial direction. During the magnetohydrodynamics evolution of the accretion disk, a mass outflow toward the direction perpendicular to the equatorial plane is driven by the activity of the accretion disk. However, the density in the vicinity of the rotation axis remains low due to the centrifugal force acting on the injected matter. Thus, the accretion of matter into the black hole proceeds primarily from the innermost region of the disk. In ideal mag-netohydrodynamics, the accretion of matter accompanies the infall of magnetic flux into the black hole. Although the magnetic field comoving with the infalling matter falls together into the black hole, the magnetic-field line outside the black hole can expand outward, in particular along the rotational axis where matter density and gas pressure are low. Such magnetic fields eventually develop a magnetosphere for which the magnetic-field lines are nearly aligned with the rotational axis (except for the vicinity of the black hole).[5] The magnetic pressure in such a region is lower than the gas pressure of the surrounding thick torus, which is formed after the activity of the accretion disk is enhanced (see the second to fifth rows of Fig. 1). In other words, the size of the magnetosphere is determined by the structure of the thick torus.

The magnetic-field lines penetrate the black hole spin-ning rapidly with the dimensionless spin $\gtrsim 0.8$, and thus, the system can be subject to the Blandford-Znajek mecha-nism [95] by which the rotational kinetic energy of the black hole is converted to the outgoing Poynting flux. In the presence of matter for which the rest-mass energy density is comparable to or larger than the electromagnetic energy density, the Poynting flux cannot propagate away effi-ciently. However, the density in the polar region decreases with time because the matter in the vicinity of the black hole falls into the black hole and a part of the matter is expelled by the magnetic pressure. Hence, eventually,

electromagnetic waves generated by the Blandford-Znajek effect can propagate away (cf. the second to fifth rows of Fig. 1). If an efficient conversion of the electro-magnetic energy of matter to kinetic energy occurs during the subsequent propagation, a gamma-ray burst jet may be launched. Since the magnetic field has a collimated structure, the electromagnetic emission is also collimated. This collimated emission continues as far as the gas pressure of the thick and dense torus confines the mag-netosphere (see Sec. III C).

We note that the evolution processes described above are qualitatively universal irrespective of the black-hole mass, initial magnetic-field strength, and grid resolution employed in this paper. In the following subsections, we describe the quantitative details of the accretion disk evolution, mass ejection, and generation of strong Poynting flux in the magnetosphere.

B. Evolution of the accretion disk and post-merger mass ejection

1. Disk evolution and ejecta

In this subsection, we present the quantitative details on the evolution of the accretion disk and the mass ejection. Figure 3 shows the rest mass of the matter located outside the apparent horizon $M_{>AH}$ (dashed curves) and the accretion disk mass M_{disk} (solid curves) as functions of time. Figure 4 shows the rest mass of the unbound matter (ejecta) M_{eje} as a function of time. These quantities are defined by

$$M_{>AH} := \int_{r>r_{AH}} \rho_* d^3x + M_{esc}, \tag{4}$$

$$M_{eje} := \int_{-hu_t>h_{min},r>r_{AH}} \rho_* d^3x + M_{esc}, \tag{5}$$

$$M_{disk} := M_{>AH} - M_{eje}, \tag{6}$$

where $\rho_* := \rho\sqrt{-g}u^t$, with g being the determinant of the spacetime metric $g_{\mu\nu}$ and u^t the time component of the four-velocity u^μ, and r_{AH} denotes the coordinate radius of the apparent horizon with respect to the black-hole puncture. M_{esc} denotes the rest mass escaping from the computational domain, which is calculated from

$$\dot{M}_{esc} := \oint \rho\sqrt{-g}u^i dS_i, \tag{7}$$

$$M_{esc} := \int^t \dot{M}_{esc}dt. \tag{8}$$

The surface integral is performed near the outer boundaries of the computational domain.

---

[5]Although we find an aligned magnetic field with constant polarity in our present simulation, it is not conclusive whether such magnetic field is always formed or not; see, e.g., Refs. [59,66,94] for related work.
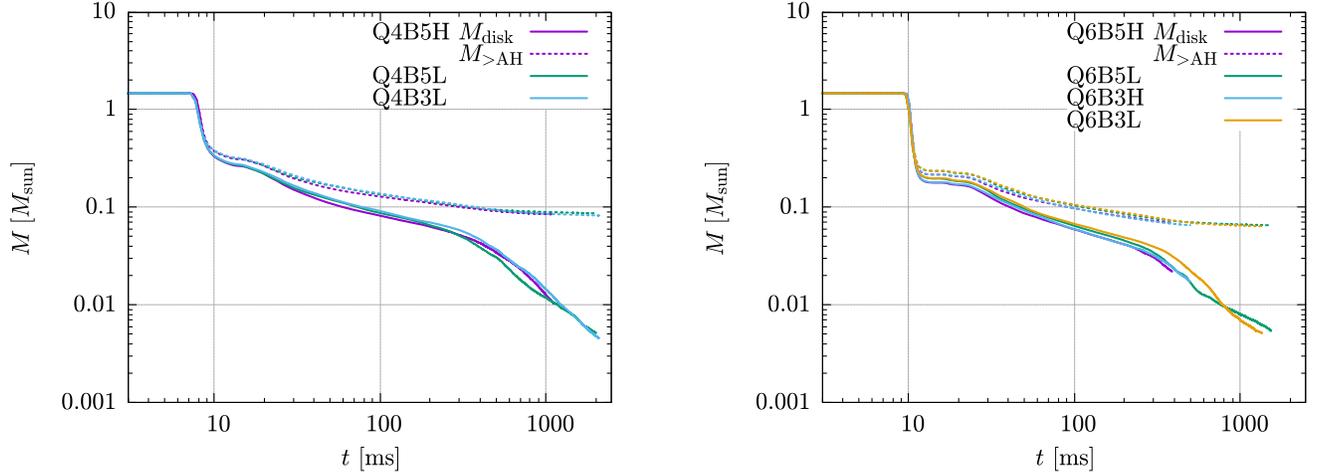
FIG. 3.   Time evolution of the rest mass of the matter located outside the apparent horizon (dashed curves) and the accretion-disk mass (solid curves) for all of the runs with $Q = 4$ (left panel) and $Q = 6$ (right panel).
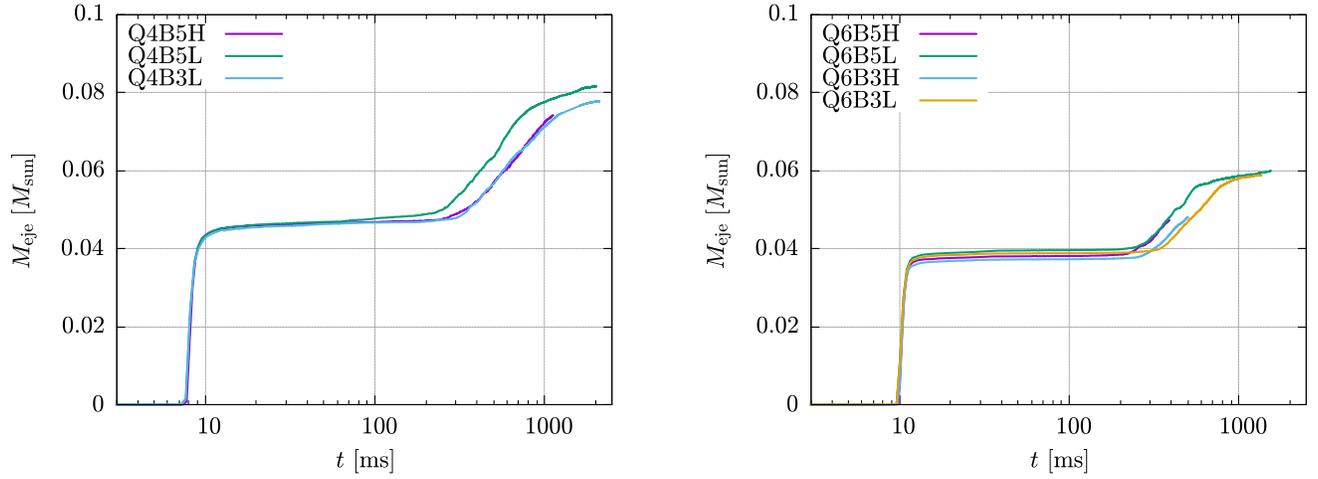

FIG. 4.   Time evolution of the rest mass of the unbound matter (ejecta) for all of the runs with $Q = 4$ (left panel) and $Q = 6$ (right panel).

The ejecta component is identified by considering the Bernoulli criterion, i.e., we regard the matter located outside the apparent horizon that satisfies $hu_t < -h_{min}$ as the unbound component. Here, $u_t(< 0)$ is the lower time component of the four-velocity and h is the specific enthalpy. h_{min} is the minimum specific enthalpy for a given electron fraction Y_e and it is obtained from the tabulated EOS employed. The value of $M_{>AH}$ for $t \lesssim 20$ ms is in approximate agreement with that in our previous paper [41] in which magnetohydrodynamics and resulting viscous effects were absent. In the present simulation, in contrast to that in Ref. [41], for $t \gtrsim 20$ ms, $M_{>AH}$ continuously decreases due to the matter accretion onto the black hole induced by the angular-momentum transport resulting from the magnetohydrodynamics effects, as already mentioned in Sec. III A. We note that the curves

of $M_{>AH}$ depend only weakly on the initial magnetic-field strength and grid resolution.

The value of M_{eje} increases steeply at two characteristic moments. The first increase is found right after the tidal disruption, and the steep increase continues only for a few ms, comparable to the dynamical time scale of the system. Thus, this mass ejection component is the dynamical ejecta. The rest mass for this component is ≈ 0.05 $M_\odot$ and ≈ 0.04 $M_\odot$ for models with $Q = 4$ and 6, respectively. The result for $Q = 4$ is in good agreement with our previous radiation-hydrodynamics result [41] because the magnetic-field strength is still weak at the tidal disruption, and hence the magnetohydrodynamics effects play essentially no role in the dynamical mass ejection. After the steep increase, the value of M_{eje} remains approximately constant for the next few hundred ms, reflecting that efficient mass

ejection activity is quiescent during this time. In this quiescent stage, however, the accretion disk is actively evolved due to the MRI and associated turbulent motion, and the density and temperature of the disk decrease (see, e.g., Fig. 5 for the rest-mass density) due to the expansion of the disk resulting from the angular-momentum transport process and enhanced magnetic pressure. As a result of the decrease in temperature, the neutrino luminosity eventually drops below the heating rate associated with the turbulent motion (cf. Fig. 6), and then the post-merger mass ejection driven by the heating associated with the MRI turbulence sets in. Thus, the second steep increase of M_{eje} that starts at $t \sim 300$–500 ms is triggered by the quick damping of the neutrino luminosity (see Fig. 6). We emphasize here that even in the presence of pure magnetohydrodynamics processes (not effectively viscous processes resulting from

the MRI turbulence), the post-merger mass ejection appreciably occurs only after this onset time and that, since the post-merger mass ejection continues for several hundred ms, simulations with durations shorter than ~ 500 ms cannot clarify this ejection process.

The rest mass of the post-merger ejecta is $\approx 0.035\ M_{\odot}$ and $\approx 0.020\ M_{\odot}$ for models with $Q = 4$ and 6, respectively, and these values are about 10% of the disk mass at its formation (at $t \sim 10$ ms). For both $Q = 4$ and 6, the dynamical ejecta is the primary component of the ejecta in the present setting, and this tendency is stronger for the larger mass ratio, as discussed, e.g., in Refs. [9,32]. The onset time of $t \sim 300$–500 ms for the post-merger mass ejection depends on the initial magnetic-field strength and grid resolution by 100–200 ms. Our interpretation of this difference is that the magnetohydrodynamics turbulence is
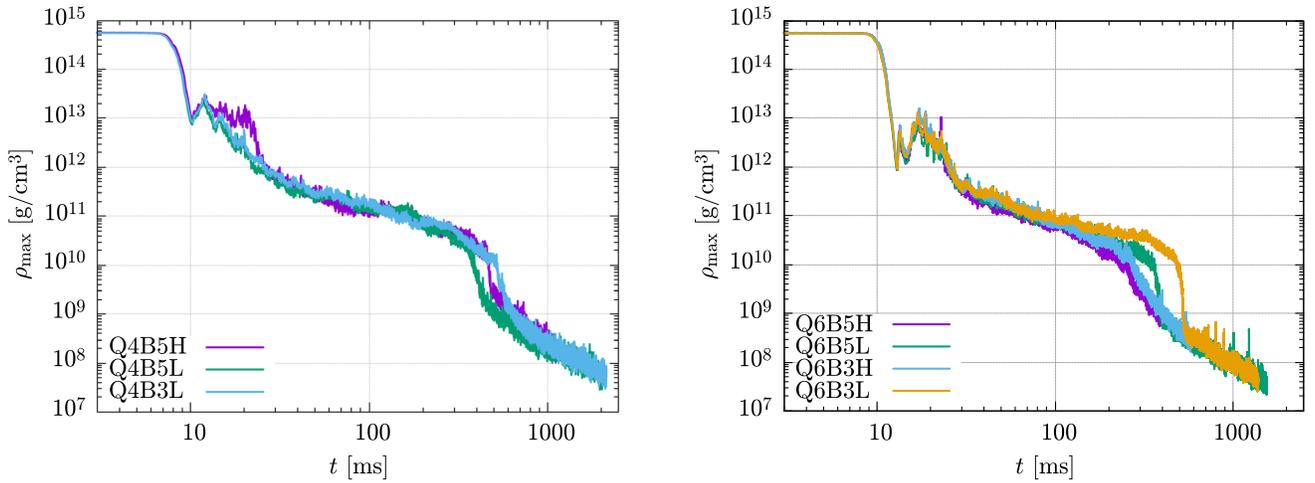

FIG. 5. Time evolution of the maximum rest-mass density of the bound matter located outside the apparent horizon for all of the runs with $Q = 4$ (left panel) and $Q = 6$ (right panel).
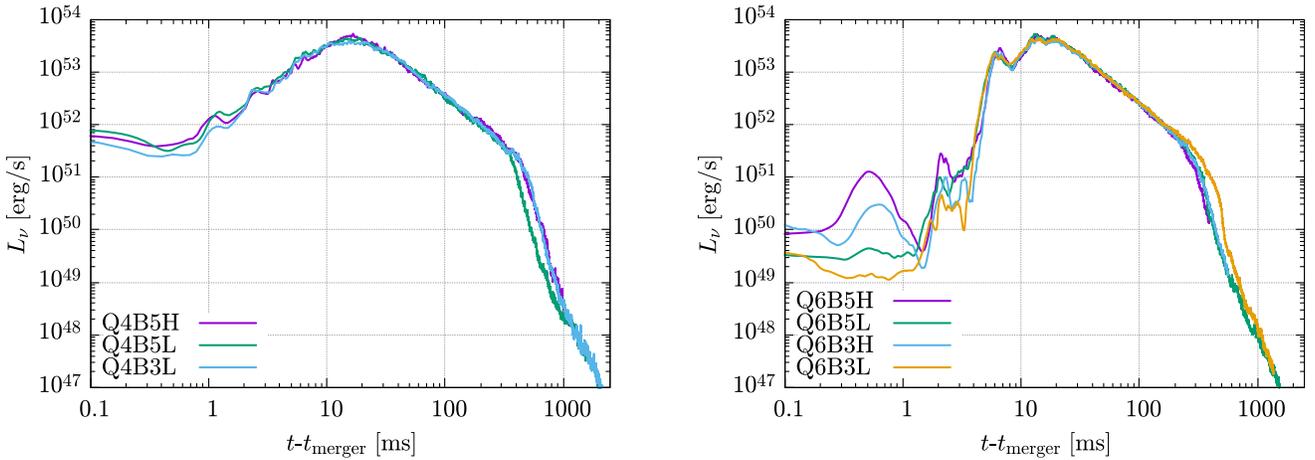

FIG. 6. Time evolution of the total neutrino luminosity (sum of the luminosity for all of the neutrino species) for all of the runs with $Q = 4$ (left panel) and $Q = 6$ (right panel). The post-merger mass ejection sets in at $t - t_{merger} \sim 300$–500 ms, at which $L_{\nu} \sim 10^{51.5}$ erg/s.

a stochastic process, and hence the angular-momentum transport process can depend on the difference in the initial-field strength and grid resolution. However, the total ejecta mass and the properties of the post-merger ejecta do not depend strongly on them (see below for the electron fraction and velocity of the ejecta).

Figures 5 and 6 display the time evolution of the maximum rest-mass density ρ_{max} and the total neutrino luminosity L_ν, respectively. To generate Fig. 6, we defined the merger time t_{merger} as the time at which the rest-mass density reaches its local minimum value for the first time, i.e., $t \approx 10$ and 13 ms for $Q = 4$ and 6, respectively. These figures indeed show that the density and neutrino luminosity decrease steeply at $t \approx 300$–500 ms. This simultaneous decrease clearly elucidates that the evolution of the accretion disk and the timing of the post-merger mass ejection are controlled by the neutrino cooling. We also note that after the onset of the post-merger mass ejection,

the accretion rate of the matter onto the black hole also decreases steeply with time; see the left panel of Fig. 7.

One interesting point is that the curve of L_ν well reflects the evolution of the accretion disk. From $t - t_{merger} \approx 1$ ms to ~ 20 ms, L_ν increases by orders of magnitude for both $Q = 4$ and 6. This reflects the temperature increase during the formation of the accretion disk (e.g., due to the compressional heating and shock heating) and the subsequent enhancement of the turbulent state in the accretion disk due to the MRI (see, e.g., Fig. 8, which shows the increase of the electromagnetic energy during this stage). Subsequently, L_ν monotonically decreases for $t - t_{merger} \gtrsim 20$ ms, because in this stage the accretion disk expands due to the angular-momentum transport process and enhanced magnetic pressure, and the density and temperature gradually decrease. However, the thermal energy generated by the heating associated with the MRI
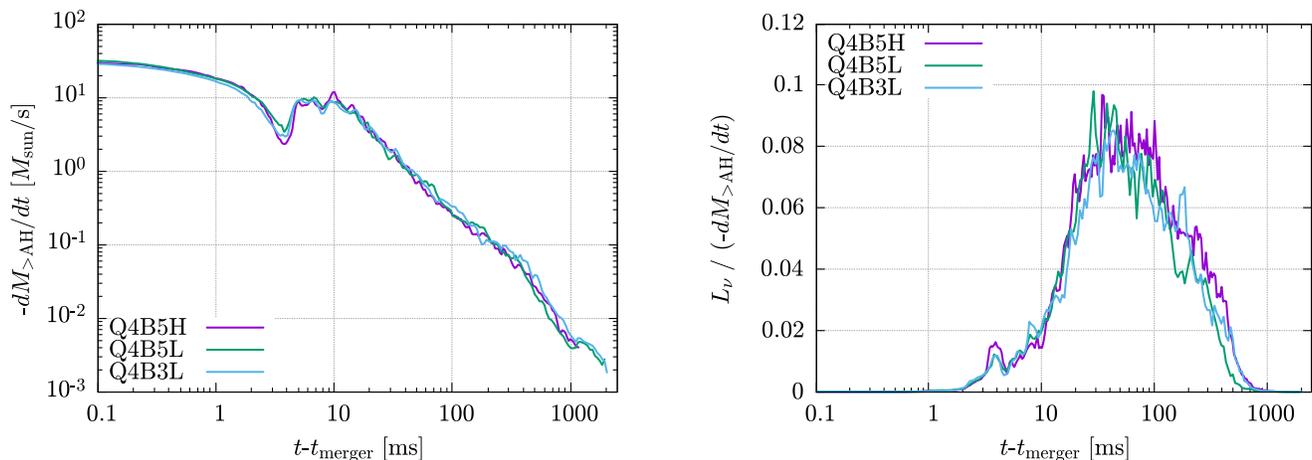

FIG. 7. Time evolution of the rest-mass accretion rate calculated from $-dM_{>AH}/dt$ (left panel) and the neutrino emission efficiency $L_\nu/(-dM_{>AH}/dt)$ (right panel) for all of the runs with $Q = 4$.
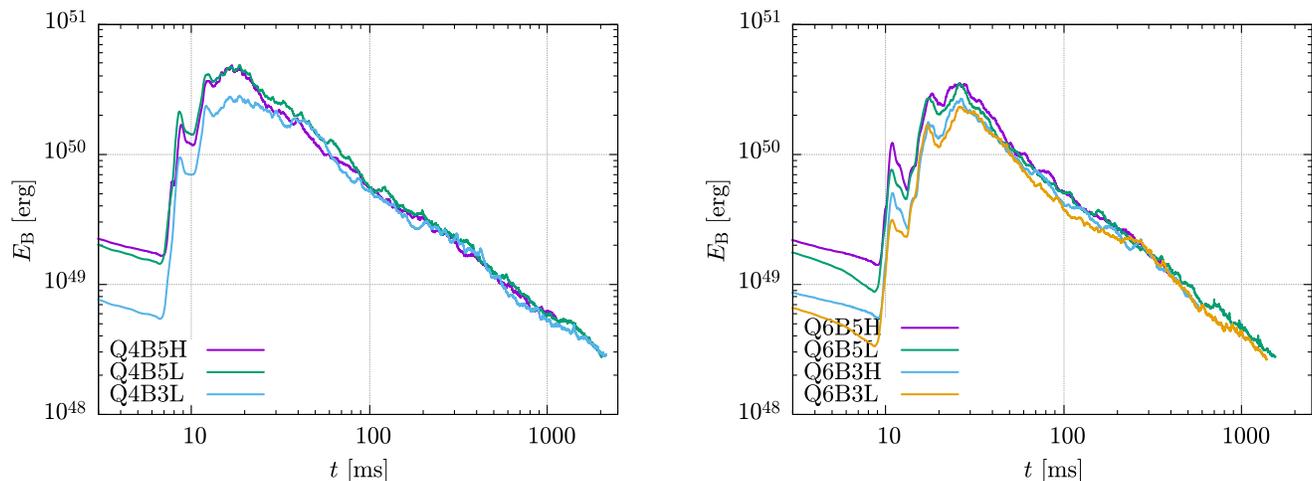

FIG. 8. Time evolution of the electromagnetic energy evaluated for the outside of the apparent horizon for all of the runs with $Q = 4$ (left panel) and $Q = 6$ (right panel).

turbulence is consumed primarily by neutrino cooling prior to the onset of the post-merger mass ejection. Hence, the expansion of the accretion disk does not proceed rapidly, and thus the mass ejection due to the thermally generated energy is suppressed. It is found that L_ν decreases approximately as $t^{-1.6}$ during this stage, and the decrease is fairly mild. However, after L_ν decreases below $\approx 10^{51.5}$ erg/s as a result of the disk expansion and resulting decrease of the temperature, the neutrino emission rate becomes smaller than the thermal energy generation rate due to the MRI turbulence. Then, the turbulent heating is used efficiently for the outward expansion of the disk, in particular through the convective motion from the inner to outer region (see footnote 1), and the post-merger mass ejection is driven. (We note that the critical neutrino luminosity, which is $\sim 10^{51.5}$ erg/s in the present case, should depend on the disk mass because the luminosity should be approximately proportional to it.) Subsequently, the neutrino luminosity exponentially drops at $t \approx 300$–500 ms irrespective of the binary mass ratio and the initial choice of the magnetic-field strength. Specifically, this post-merger mass ejection sets in when the temperature for most of the disk matter decreases below ~ 3 MeV (cf. the top panel of Fig. 10 for a mass distribution with respect to the temperature as a function of time). This critical temperature at the onset of the post-merger mass ejection is quantitatively the same as that found in general-relativistic neutrino-radiation viscous hydrodynamics simulations of black hole–torus systems [61,62]. However, the time of onset of the post-merger mass ejection is earlier than that in the viscous hydrodynamics result for similar black-hole mass cases [62]. As indicated in Refs. [53,59,66], inherent magnetohydrodynamics effects such as the magneto-centrifugal effect [91] are likely to accelerate the mass ejection from the disk. The neutrino luminosity of $\approx 10^{51.5}$ erg/s at the onset of the

post-merger mass ejection that we find in this paper is indeed similar to that found in our recent magnetohydrodynamics study [66].

Figure 7 plots the rest-mass accretion rate onto the black hole calculated using $-dM_{>\mathrm{AH}}/dt$ and the neutrino emission efficiency defined by $L_\nu/(-dM_{>\mathrm{AH}}/dt)$. After the early matter infall associated with the onset of the merger, the mass accretion rate has a peak at $t - t_{\mathrm{merger}} \sim 10$ ms. This is due to the fact that the magnetic-field strength is amplified in the accretion disk and the mass accretion rate is enhanced (cf. Fig. 8). After the peak, the mass accretion rate decreases monotonically with time approximately as $\propto t^{-2}$ for $t - t_{\mathrm{merger}} \lesssim 50$ ms and as $\propto t^{-1}$ in the subsequent stage before the onset of the post-merger mass ejection. After the onset of the post-merger mass ejection, the mass accretion rate drops steeply. Broadly speaking, the curve of the neutrino emission efficiency reflects that of L_ν. However, the peak comes at $t - t_{\mathrm{merger}} \sim 40$–50 ms, which is slightly later than the peak time of the neutrino luminosity and mass accretion rate. The reason for this is that $L_\nu \propto t^{-1.6}$, while $-dM_{>\mathrm{AH}}/dt \propto t^{-2}$ for $t - t_{\mathrm{merger}} \lesssim 50$ ms and subsequently $-dM_{>\mathrm{AH}}/dt \propto t^{-1}$, and thus the peak is shifted at $t - t_{\mathrm{merger}} \sim 50$ ms. The maximum neutrino emission efficiency is ~ 8–10%. Keeping the difference in the disk mass in mind, this value agrees broadly with those found in our viscous hydrodynamics simulations for similar black-hole mass ($M_{\mathrm{BH}} = 6\ M_\odot$) and dimensionless spin ($\chi_{\mathrm{BH}} = 0.8$) [62].

2. Magnetic-field evolution

Figures 8 and 9 show the time evolution of the electromagnetic energy E_{B} and the ratio of the electromagnetic energy to the internal energy E_{int}, respectively. Here, E_{B} and E_{int} are defined by
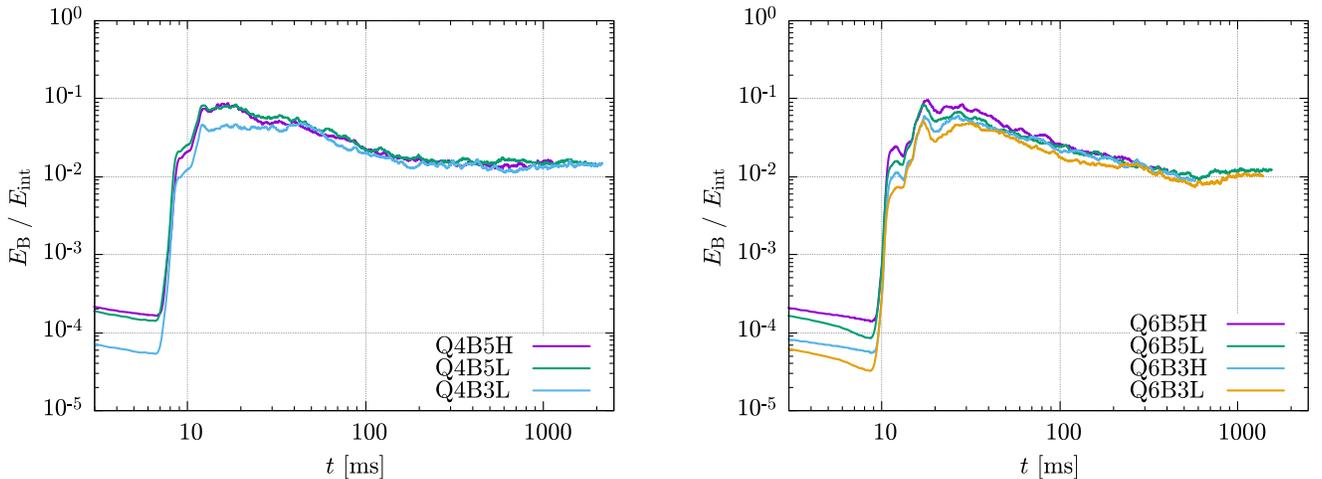

FIG. 9. Time evolution of the ratio of the electromagnetic energy to the internal energy evaluated for the outside of the apparent horizon for all of the runs with $Q = 4$ (left panel) and $Q = 6$ (right panel).
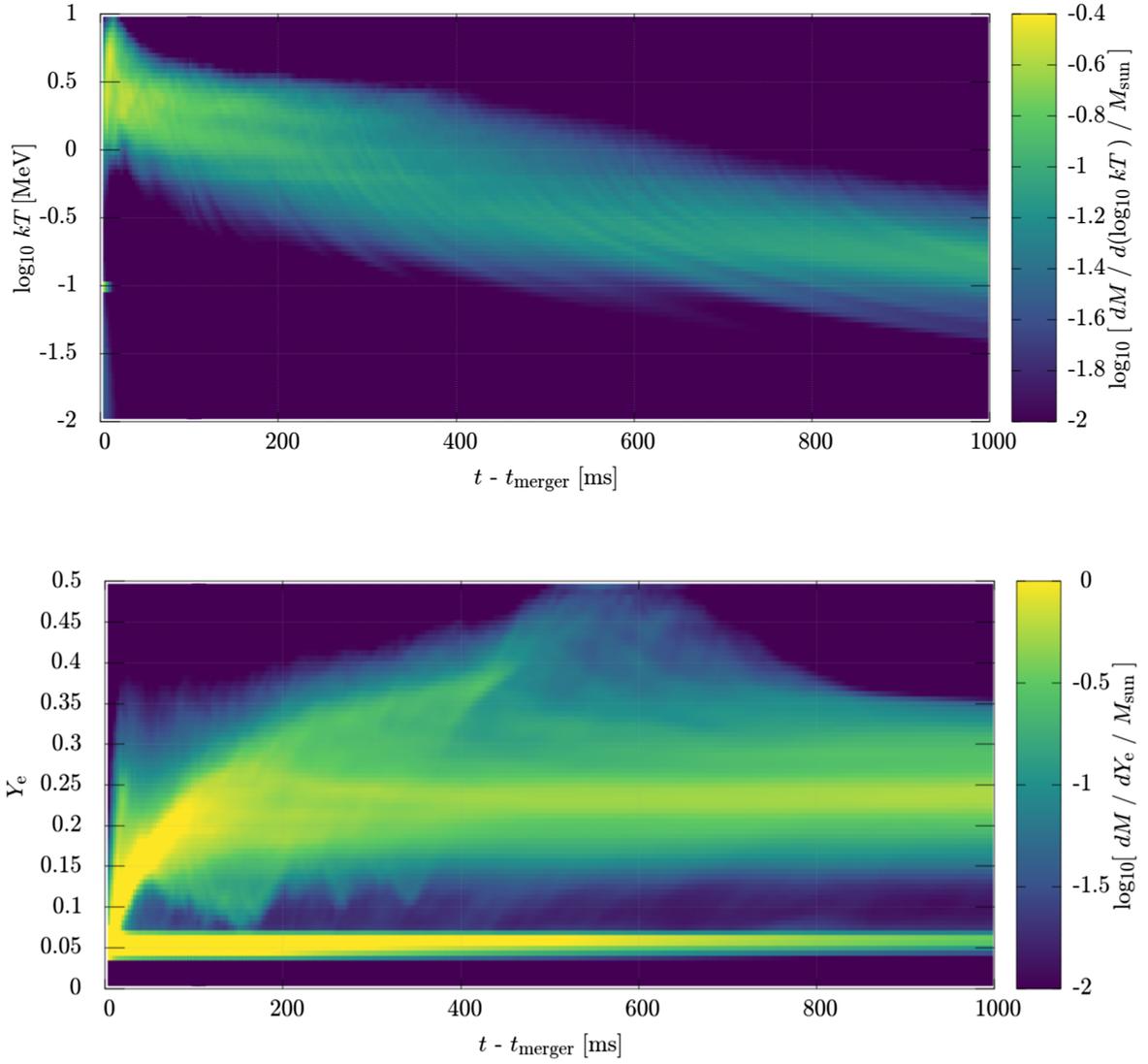
FIG. 10.   Time evolution of the mass histograms with respect to the temperature (upper panel) and electron fraction (lower panel) for model Q4B5H. The post-merger mass ejection sets in when the temperature for most of the matter decreases below 3 MeV at $t \sim 400$ ms for this model. Note that only matter in the computational domain is taken into account in this figure, and thus matter that has escaped from the computational domain is neglected in the late stages. Thus, for $t \gtrsim 300$ ms the dynamical ejecta mass decreases with time.

$$E_{\mathrm{B}} := \frac{1}{8\pi} \int_{r > r_{\mathrm{AH}}} u^t \sqrt{-g} b_\mu b^\mu d^3 x, \qquad (9)$$

$$E_{\mathrm{int}} := \int_{r > r_{\mathrm{AH}}} \rho_* \varepsilon d^3 x, \qquad (10)$$

and ε denotes the specific internal energy. Here we note that the energy-momentum tensor in the ideal magnetohydrodynamics is written as

$$
\begin{aligned}
T_{\mu\nu} = {} & \rho h u_\mu u_\nu + P g_{\mu\nu} \\
& + \frac{1}{4\pi} \left(b^\alpha b_\alpha u_\mu u_\nu + \frac{1}{2} b^\alpha b_\alpha g_{\mu\nu} - b_\mu b_\nu \right), \qquad (11)
\end{aligned}
$$

and with $h = c^2 + \varepsilon + P/\rho$, we have

$$u^t \sqrt{-g} T_{\mu\nu} u^\mu u^\nu = \rho_*(c^2 + \varepsilon) + \frac{1}{8\pi} u^t \sqrt{-g} b^\mu b_\mu. \qquad (12)$$

Here we recover c to clarify the physical units. Thus, the choice of E_{int} and E_{B} stems from Eq. (12).

During the merger stage, the magnetic-field strength in the accretion disk is amplified quickly on a short time scale of a few ms. This is initially induced by the magnetic winding associated with the differential rotation in the accretion disk. In the Keplerian disk in the presence of the poloidal magnetic field of the cylindrically radial component B^ϖ, the strength of the toroidal magnetic field B^T increases approximately linearly with time until saturation as (e.g., Ref. [96])

$$B^T \approx \frac{3}{2} B^\varpi \Omega t, \tag{13}$$

where Ω denotes the local angular velocity. For a black hole with a dimensionless spin of 0.8, the angular velocity at the innermost stable circular orbit of the black hole is $\Omega_{\text{ISCO}} \approx 0.174 M_{\text{BH}}^{-1} \approx 5.43 \times 10^3 (M_{\text{BH}}/6.5 M_\odot)^{-1}$ rad/s [97]. Thus, for the models of $Q = 4$ and $Q = 6$, the matter near the innermost stable circular orbit rotates with an orbital period of ≈ 1.2 and 1.6 ms, respectively. This implies that in the first ~ 10 ms, the toroidal field strength can be ~ 60–80 times B^ϖ, the maximum of which is $\sim 10^{14}$ G at the formation of the accretion disk (i.e., much weaker than the field strength in the neutron star initially given) in the present simulations. This is the reason that the initial steep amplification to $E_B > 10^{50}$ erg is found in our present simulations. Because the winding time scale is quite short, the magnetic-field amplification by ~ 3 orders of magnitude in $\lesssim 100$ ms is possible even in the absence of other instabilities such as MRI; even for an initial value of $B^\varpi = 10^{12}$ G, the toroidal field can be amplified to $\sim 10^{15}$ G in ~ 100 ms. After sufficient amplification of the toroidal magnetic field, an outward expansion of the accretion disk is driven toward the polar direction due to the enhanced magnetic pressure, and a poloidal field with strength comparable to that of the toroidal field is also generated. We note that the Kelvin-Helmholtz instability that takes place during the winding of the spiral arm around the black hole and collision between different parts of the spiral arm may also partly contribute to the magnetic-field amplification.

After the initial amplification of the magnetic-field strength, the ratio of E_B/E_{int} reaches ~ 0.05–0.1. Then, the magnetic-field growth is saturated. The electromagnetic energy at the saturation, $E_{B,\text{sat}}$, is smaller for smaller values of the initial magnetic-field strength. However, the relative difference in the saturated electromagnetic energy between models with different initial magnetic-field strengths is not as large as that in the initial electromagnetic energy. Furthermore, the electromagnetic energy for $t \gtrsim 30$ ms depends only weakly on the initial condition (as well as on the grid resolution). Thus, we infer that the amplification and saturation of the magnetic-field strength take place in a universal manner irrespective of the initial magnetic-field strength.

When reaching saturation, a typical magnetic-field strength is 10^{15} G (cf. Fig. 2) and the maximum rest-mass density is $\sim 10^{11}$–10^{12} g/cm^3 in the innermost region. Thus, the Alfvén velocity is $\approx b/\sqrt{4\pi\rho} \approx 9 \times 10^8$ cm/s $(b/10^{15}$ G$)(\rho/10^{11}$ g cm$^{-3})^{-1/2}$ and the wavelength of the fastest growing mode of the MRI is typically ~ 10 km [86]. As a result, the wavelength of this unstable mode is covered by tens of grid points in

our setting (see Appendix C), and hence the effect of the MRI subsequently comes into play. With the evolution of the disk, the typical magnetic-field strength and rest-mass density decrease, but in the equipartition stage (see below) the Alfvén velocity is always of order $\sqrt{E_B/E_{\text{int}}}(\sim 10\%)$ of the sound speed, which changes weakly with time. Thus, the wavelength of the fastest growing mode of the MRI is always covered by tens of grid points in the present setting. Indeed, our numerical analysis shows that the wavelength is covered by ~ 10 grid points for the region with $\rho = 10^{11}$ g/cm^3, and more (several tens of) grid points for the lower-density region.

After the MRI starts to play a role, a turbulent state is developed in the accretion disk and an effective viscosity is induced. We evaluate the following ratio of the anisotropic stress to the pressure:

$$\alpha_{ij} := \left\langle \left| \frac{1}{P}\left(\rho h \hat{u}_i \hat{u}_j - \frac{1}{4\pi} b_i b_j \right) \right| \right\rangle_{\text{ave}}, \tag{14}$$

where $i \neq j$ ($i, j = x, y, z$) and $\langle \cdots \rangle_{\text{ave}}$ denotes the spatial average with the weight of the rest-mass density (ρ_*) for the region with $z \geq 0$ and $\rho \geq 10^7$ g/cm^3. $\hat{u}_i$ is defined by $u_i - \langle u_i \rangle_{t,\text{ave}}$, where $\langle u_i \rangle_{t,\text{ave}}$ denotes the local time average of u_i. The time average needs to be subtracted from u_i to eliminate the contribution of coherent motion (not random motion) for evaluating the anisotropic stress associated with the turbulent motion. We find that all of the components of α_{ij} are between ≈ 0.02 and 0.1 at the onset of the post-merger mass ejection depending only weakly on the initial magnetic-field strength and grid resolution. The values of α_{ij} are comparable to the viscous alpha parameter often employed in viscous hydrodynamics simulations (e.g., Refs. [57,61,62]). The value is slightly larger than the result of previous magnetohydrodynamics simulations of black-hole accretion disks [98], but this difference likely comes from the difference in the definition of α_{ij}. At this stage, the ratio of E_B/E_{int} settles to $O(10^{-2})$.

As a result of the viscous angular-momentum transport, the matter in the inner region of the accretion disk falls into the black hole while the matter in the outer part expands outward. Because of the matter infall into the black hole, the rest mass of the accretion disk decreases (see Fig. 3) and, associated with the decrease in the rest mass, the electromagnetic energy decreases with time, although the ratio of $E_B/E_{\text{int}} = O(10^{-2})$ is preserved. Thus, for $t \gtrsim 100$ ms, the accretion disk is in a quasisteady equi-partition state: the magnetic-field energy relaxes to $\sim 1\%$ of the internal energy irrespective of the mass and internal energy of the accretion disk. It is interesting to point out that the electromagnetic energy decreases approximately in proportion to t^{-1}. All of these features are found for the models of both $Q = 4$ and $Q = 6$ irrespective of the initial magnetic-field strength and grid resolution.

3. Properties of ejecta

Now we turn our attention to the properties of the ejecta. The bottom panel of Fig. 10 displays the mass distribution of the remnant matter with respect to the electron fraction Y_e for model Q4B5H. This shows that there are two characteristic peaks of Y_e in regions around 0.05 and 0.25–0.35, respectively. The former peak is associated primarily with the dynamical ejecta and the latter with the accretion disk for $t \lesssim 400$ ms and post-merger ejecta for $t \gtrsim 400$ ms. This figure clearly shows that the dynamical ejecta component with $Y_e = 0.03$–0.07 comes directly from the neutron star, because the values are unchanged from the beginning. That is, this dynamical ejecta component is not essentially affected by thermal or weak-interaction processes during the merger and post-merger stages.

By contrast, the electron fraction of the post-merger ejecta is found to be determined by the evolution process of the accretion disk, in which the typical electron fraction increases from ~0.05 to ~0.25 for $0 < t \lesssim 200$ ms. As already mentioned, at this stage the accretion disk gradually expands due to the viscous and magnetohydrodynamical angular-momentum transport and magnetic pressure by the amplified magnetic-field strength, and its rest-mass density

and temperature monotonically decrease. In the disk with its optical depth to neutrinos $\lesssim 1$, the electron fraction is determined predominantly by the reaction equilibrium between electron/positron capture reactions if the temperature is high enough (typically $kT \gtrsim 2$–3 MeV; see Refs. [62,65,99]) for their time scale to be shorter than that of the disk expansion. Due to the disk expansion, the electron degeneracy becomes weak, and as a result the electron fraction is shifted to higher values in the reaction equilibrium state. With the decrease of the temperature, the neutrino luminosity decreases approximately in proportion to T^6. As already mentioned, the post-merger mass ejection sets in when the neutrino luminosity drops below $\sim 10^{51.5}$ erg/s, which occurs for $t \gtrsim 300$ ms. The typical value of Y_e for the post-merger ejecta is determined around this timing, resulting in $Y_e \approx 0.25 \pm 0.10$.

Figure 11 shows the rest-mass histograms as functions of the electron fraction and velocity for the ejecta component for the models for which the simulation time is longer than 1 s. The mass histograms are derived for the ejecta which escapes away from a sphere with the radius of $\approx 10^4$ km. As described in the previous paragraphs, there are two distinct Y_e components for the ejecta, and this feature is clearly observed in Fig. 11. The dynamical ejecta component
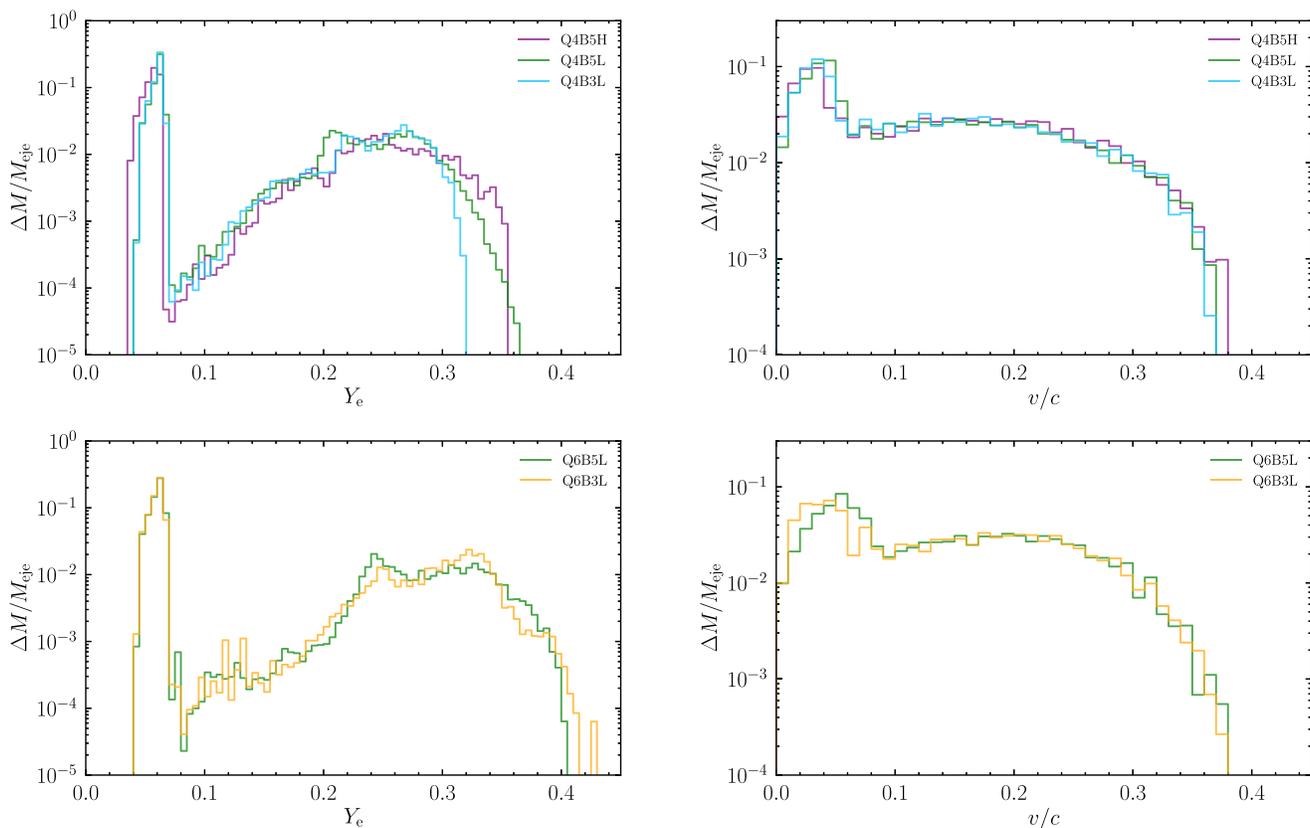

FIG. 11. Mass histograms as functions of the electron fraction (left panels) and velocity (right panels) of ejecta for the models with simulation time longer than 1 s (models Q4B5H, Q4B5L, Q4B3L, Q6B5L, and Q6B3L). Models with $Q = 4$ and $Q = 6$ are displayed in the upper and lower panels, respectively.

always has $Y_e \approx 0.03$–0.07 irrespective of the black-hole mass. By contrast, the distribution of Y_e for the post-merger ejecta component depends on the black-hole mass in the present results. Specifically, for larger black-hole mass, the value of Y_e tends to be larger. As a result, the peak of Y_e changes from ~ 0.25 for $Q = 4$ to ~ 0.31 for $Q = 6$. This is in agreement with our findings in our viscous hydro-dynamics studies [62] (see also Refs. [64,65]). The reason is as follows: under the condition that the disk mass has an approximately identical value, the density of the disk can be higher for the lower black-hole mass (the lower mass ratio Q in the present context), because the tidally disrupted matter can have a more compact orbit around the black hole due to the smaller radius of its innermost stable circular orbit. Associated with this effect, the temperature is enhanced due to compression and stronger shock heating, resulting in a higher neutrino emissivity and reducing the entropy per baryon of the matter in the accretion disk (cf. Fig. 6). With the lower entropy per baryon, the degree of electron degeneracy becomes higher and neutron rich-ness is enhanced. Therefore, for the lower black-hole mass, the electron fraction of the post-merger ejecta becomes slightly lower. Figure 11 shows that this effect is found irrespective of the initial-magnetic field strength and grid resolution (and thus it is physical).

The right panels of Fig. 11 show the rest-mass histogram as a function of the ejecta velocity. Again, there are two components. Here, the low-velocity component with $v/c \lesssim 0.08$ stems primarily from the post-merger ejecta, while the high-velocity component stems from the dynami-cal ejecta. We note that the velocity distribution for the dynamical ejecta is in good agreement with that in our previous study [41], and the typical velocity of the post-merger ejecta agrees approximately with that found in viscous hydrodynamics simulations (e.g., Refs. [61,62]). As we reported in Ref. [32], the velocity of the dynamical ejecta is at most $\sim 0.4c$. This is in contrast to the case of binary neutron star mergers in which the maximum ejecta velocity can be $\gtrsim 0.8c$ [100].

Our present results confirm that there are two distinct ejecta components—a low-Y_e and high-velocity component, and a relatively high-Y_e and low-velocity component—as many previous numerical works have suggested. By our self-consistent simulations, two components emerge clearly. The former (dynamical ejecta) will likely synthesize heavy r-process elements, while the latter (post-merger ejecta) will likely synthesize relatively light r-process elements as well as heavy ones (e.g., Refs. [53,101]). Then, the former component would likely shine as a red kilonova, while the latter would likely contribute to a blue-kilonova component [52]. However, a detailed light curve and spectrum are determined by a nontrivial radiation transfer effect [102]. It is also likely that the light curve depends on the mass ratio Q. Thus, a nucleosynthesis calculation and radiation transfer simulation are topics to be explored as follow-up work.

C. Magnetic field in the funnel region and the relation to short gamma-ray bursts

In addition to the aforementioned ejected matter (dynamical and post-merger ejecta), we find a launch of a matter outflow and Poynting flux in the narrow funnel region established near the rotational axis of the black hole (see Fig. 12). In particular, the isotropic Poynting lumi-nosity estimated for most of the runs is comparable to the typical luminosity of short-hard gamma-ray bursts [11,12]. In this section, we discuss the quantitative details of this result.

Irrespective of the black-hole mass, initial magnetic-field strength, and grid resolution, tidal disruption of the neutron star takes place in our present setting and a magnetized accretion disk is formed around the central black hole. As already mentioned in the previous subsections, the mag-netic-field strength in the accretion disk is increased by the winding and MRI, and then a turbulent state is established at ~ 30–40 ms after the tidal disruption. Subsequently, the accretion disk evolves primarily due to the viscous effect stemming from the MRI turbulence. As already mentioned in the previous subsection, the magnetic-field strength is determined by an equipartition state, i.e., by the internal energy of the matter, which is typically ρc_s^2, where c_s is the
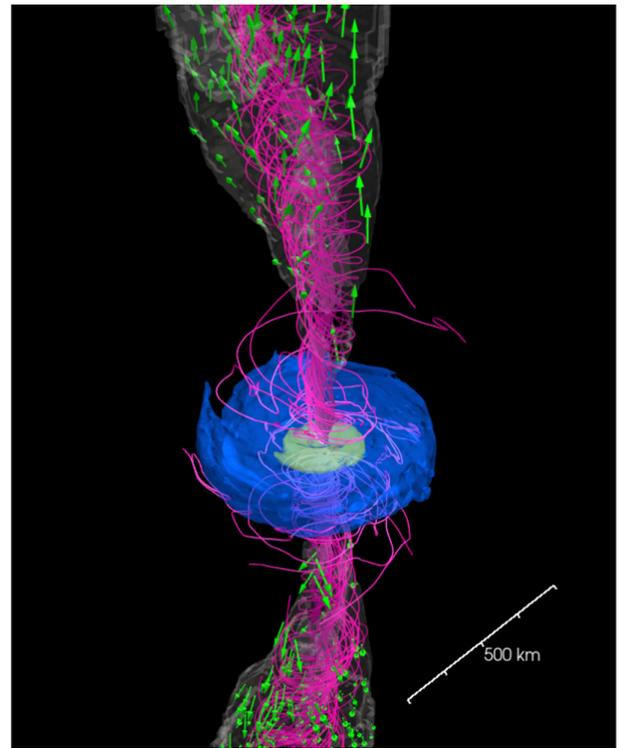

FIG. 12. Snapshots of the rest-mass density profile (blue and green contours) with the magnetic-field lines (pink curves), unbound matter (white color) and its velocity (green arrow) for model Q4B5L at $t = 300$ ms. Magnetic-field lines penetrat-ing the black-hole horizon are displayed. See also the following link for the time evolution: Ref. [103].

sound speed of order 10^9 cm/s in the dense region of the disk. Since E_B/E_{int} is of $O(10^{-2})$, the magnetic-field strength can be approximated as $\sim 0.1\sqrt{8\pi\rho c_s^2} \sim 5 \times 10^{14}(\rho/10^{12} \text{ g cm}^{-3})^{1/2}(c_s/10^9 \text{ cm s}^{-1})$ G near the inner edge of the accretion disk. The order of this magnetic-field strength is indeed found in the accretion disk (see, e.g., Fig. 2). By angular-momentum transport, the matter in the innermost part of the accretion disk falls continuously into the black hole, and during this infall the magnetic fluxes also fall in. As a result, the poloidal magnetic-field lines for which the field strength is $\gtrsim 10^{14}$ G at the horizon penetrate the black hole. Here, the infall magnetic fluxes do not have aligned polarity because the accretion process is determined by the turbulence in the accretion disk, and hence the magnetic-field strength on the horizon does not monotonically increase. On the other hand, the poloidal magnetic fields in the polar region are twisted by the black-hole spin, and hence the field strength could be larger than that for the accretion disk in the presence of a rapidly spinning black hole. Due to the twisting associated with the black-hole spin, the toroidal magnetic-field strength dominates over the poloidal one in the vicinity of the black hole (cf. Fig. 12).

However, such amplified magnetic fields do not immediately form a global magnetosphere. The reason for this is that at tidal disruption, a dense atmosphere ($\rho \sim 10^7$ g/cm^3) is formed in the polar region by the matter expelled by shocks generated during the winding and shock heating in the spiral arm. The matter also comes from the accretion disk due to its turbulent activity. Although a part of the matter in the polar region near the black hole eventually falls into the black hole, a certain fraction of the matter has to be expelled by the magnetic force to form a low-density magnetosphere. For this, the toroidal magnetic field amplified by the twisting due to the black-hole spin plays an important role, because a tower-like outflow is driven from the neighborhood of the black hole by this magnetic effect [43]. Hence, eventually, the matter energy density decreases below the magnetic energy density of $b^2/8\pi$ in the polar region of the black hole. This is satisfied for $\rho < b^2/8\pi c^2 = 4.4 \times 10^5 (b/10^{14} \text{ G})^2$ g/cm^3. Then, the magnetic pressure pushes the matter toward the outward direction along the rotation axis, establishing a low-density region near the rotational axis. During this process, the magnetic-field lines also expand outward, and a large-scale magnetosphere near the rotational axis is formed. In this region, the poloidal field is dominant (see Fig. 12). As a result, the rest-mass density decreases in the black-hole polar region, leading to the formation of the so-called funnel structure. At the funnel wall, the magnetic pressure is lower than the gas pressure of the surrounding thick torus and envelope, and hence the magnetosphere is sustained by the surrounding matter.

Inside the funnel wall, the electromagnetic energy dominates over the rest-mass energy, and thus an approximately force-free magnetosphere is formed. Here, the typical ratio of the electromagnetic energy density to the rest-mass energy density is 10–100. In such a region, the rotational kinetic energy of the black hole is extracted by the Blandford-Znajek mechanism [95] and transformed into the Poynting flux which propagates outward (see Appendix D for the result that shows the presence of the outgoing energy flux from the black hole). Figure 13 shows the time evolution of L_{iso}, an isotropic Poynting luminosity, which we define using the Poynting luminosity for $\theta < 10°$ and $r \approx 1500$ km as

$$L_{iso} := \frac{2}{1-\cos(10°)} L_{\theta<10°,r\approx1500 \text{ km}}, \qquad (15)$$

where

$$L_{\theta<10°,r\approx1500 \text{ km}} := -\int_{\theta<10°,r\approx1500 \text{ km}} T^{(EM)}{}_t{}^r \sqrt{-g} dS_r. \qquad (16)$$
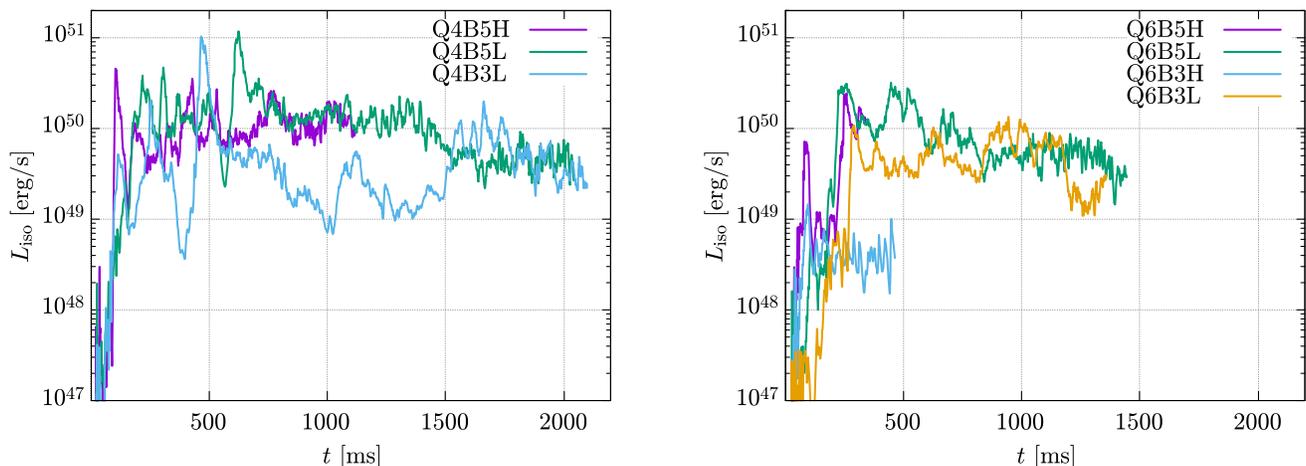

FIG. 13. L_{iso} as a function of time for all of the runs with $Q = 4$ (left panel) and 6 (right panel). The Poynting luminosity is evaluated at $r \approx 1500$ km for all of the runs.

$T_{\mu\nu}^{(EM)}$ denotes the electromagnetic part of the energy-momentum tensor. Here we choose a particular value (10°) for the surface integral because the opening angle of the funnel region is initially as narrow as $\sim 10°$ (see Figs. 14 and 15).

Figure 13 shows that the typical maximum value of L_{iso} is of order 10^{50} erg/s and L_{iso} varies with time irrespective of the black-hole mass and initial magnetic-field strength. This varying isotropic luminosity together with the opening angle of $\theta \sim 10°$ (cf. Fig. 15) is in a fair agreement
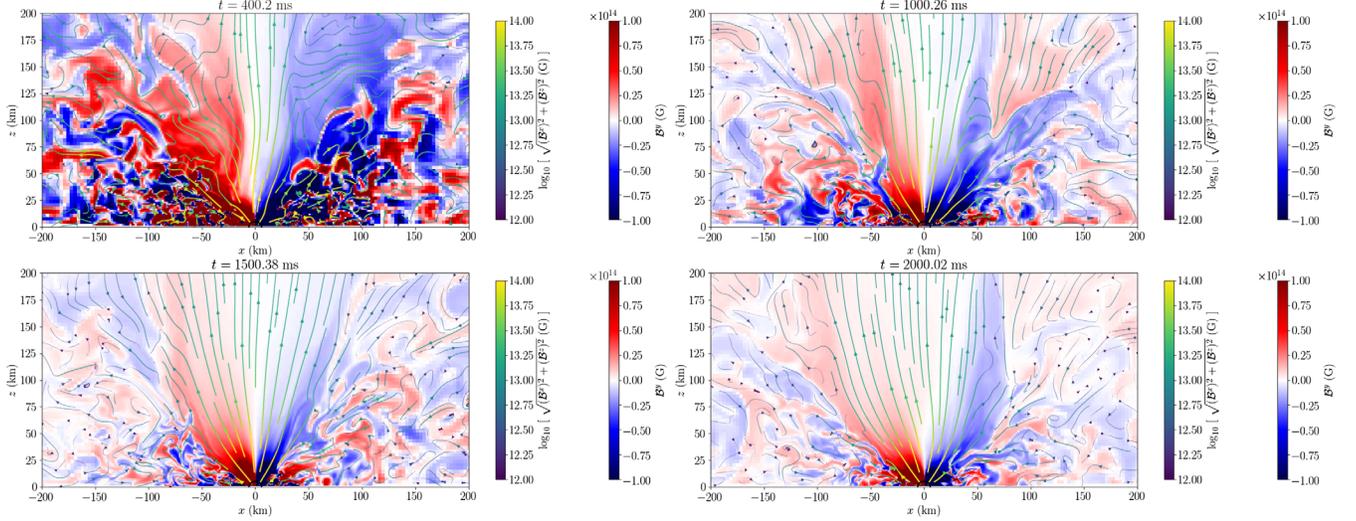

FIG. 14.   Snapshot of the toroidal magnetic field together with the poloidal magnetic-field lines (curves) in the $x - z$ plane at selected time slices for model Q4B5L. See also the following link for an animation: Ref. [104].
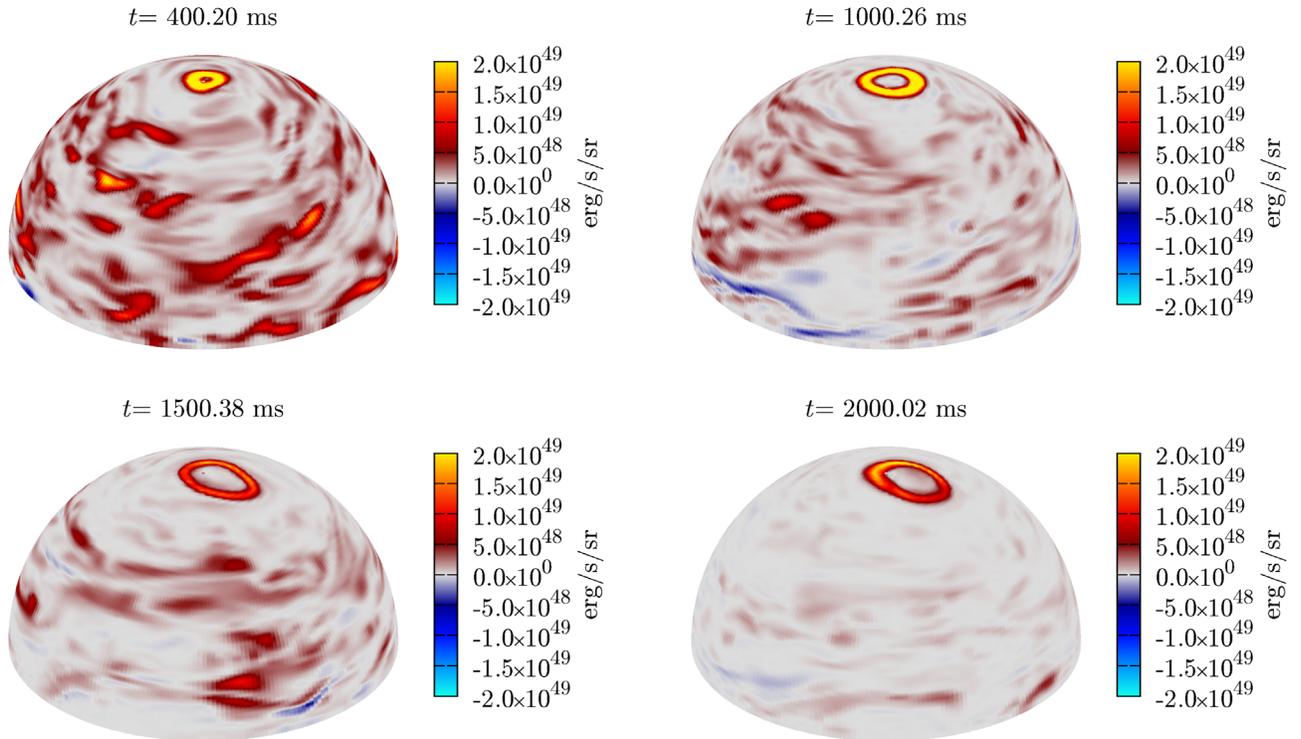

FIG. 15.   Angular distribution of the Poynting flux per steradian on a sphere of $r \approx 1500$ km for model Q4B5L at selected time slices. The bright color displayed in the polar region stems from the Blandford-Znajek effect, while for other regions the magnetic fields accompanying the outflowing matter contribute mainly to the Poynting flux. The opening angle of the Poynting flux in the polar region is shown to increase with time. See the following link for an animation: Ref. [105].

with those for short-hard gamma-ray bursts under the assumption that the conversion efficiency of the Poynting flux to the gamma-ray radiation is sufficiently high (i.e., close to unity) [11,12].[6]

The stage with a high value of $L_{\mathrm{iso}} \gtrsim 10^{50}$ erg/s continues broadly for 1 s. Subsequently, the isotropic luminosity starts to decrease. This is due to the fact that the opening angle of the funnel region increases and the magnetic-flux density is reduced. Remember that the funnel region is determined by the gas pressure of the thick torus at the funnel wall. In the long-term evolution of the accretion torus, the rest-mass density and associated gas pressure around the funnel wall decrease with time due to the post-merger mass ejection. On the other hand, the total magnetic flux penetrating the black hole does not significantly decrease in the ideal magnetohydrodynamics, and thus the decrease in the magnetic pressure is not as significant as the gas pressure at the funnel wall. Thus, as the rest-mass density decreases, the magnetic pressure exceeds the gas pressure at the original position of the funnel wall, and as a result the funnel wall expands gradually.

Figure 14 shows snapshots of the toroidal magnetic field together with the poloidal magnetic-field lines in the x-z plane at selected time slices. This indeed shows that the configuration of the magnetic-field lines changes from an aligned collimated one near the rotational axis to a more spread out one for late time with $t \gtrsim 1$ s.

Since the collimation of the poloidal magnetic-field lines is loosened, the Poynting flux in the vicinity of the rotational axis also decreases gradually. Figure 15 shows that the opening angle of the strong Poynting-flux ($-T^{\mathrm{(EM)}}{}_t{}^r \sqrt{-g}$) region increases from $\lesssim 10°$ to $\sim 20°$ and the intensity of the Poynting flux becomes weak with time. The reason that the peak of the Poynting flux is located near the funnel wall is that the magnetic-field lines near the funnel wall penetrate the equatorial regions of the spinning black hole, and hence the Blandford-Znajek effect can be more efficient. If the Poynting flux indeed determines the luminosity of short-hard gamma-ray bursts, its brightness also should decrease for $t \gtrsim 1$ s. This mechanism could be interpreted as a reason that the time scales of short-hard gamma-ray bursts are less than 2 s, with a typical time scale of ~ 1 s. Specifically, our numerical results propose that the time scale of ~ 1 s is determined by the evolution time scale of the accretion disk (torus), which is determined by the neutrino cooling and magnetohydrodynamics turbulence (effectively viscous process) that control the post-merger mass ejection.

A word of caution is appropriate here. First, the turbulence and dynamo activated by the MRI in the accretion disk are stochastic processes. This implies that the poloidal magnetic-field flux penetrating the black hole could not be precisely predicted. For example, by the accretion of the magnetic fields with a random polarity, the magnetic flux that penetrates the black hole may be smaller than that in the accretion disk. Hence, it is reasonable that the magnetic-field strength could not always be as strong as that necessary to explain typical short-hard gamma-ray bursts. Indeed, for model Q6B3H, the Poynting luminosity is 1 order of magnitude lower than those for other models. In this case, the magnetic-field strength on the black-hole horizon is about 1/3 of those for other models. Therefore, broadly speaking, there are two possible cases. 1) A magnetosphere with strong poloidal magnetic fields is formed near the rotational axis of a spinning black hole. In this case, the maximum isotropic Poynting luminosity of $10^{50} – 10^{51}$ erg/s consistent with typical short-hard gamma-ray bursts can be generated. 2) Due to the stochastic process of the MRI-induced turbulent motion, poloidal magnetic fluxes falling from the disk are not aligned well, and the poloidal magnetic field formed around the black hole is not strong enough to appreciably form a magnetically supported funnel structure (force-free magnetosphere). In such a case, the isotropic Poynting luminosity may not be high enough to be consistent with typical short-hard gamma-ray bursts, although a weak Poynting luminosity can be generated as in model Q6B3H. For a more detailed understanding on this problem, a larger number of higher-resolution simulations will be necessary. However, this is far beyond the scope of this paper with the current computational resources.

The accretion disks that we find in our simulations do not satisfy the condition for the magnetically arrested disk [106]. We calculate the total magnetic flux on the upper hemisphere of the horizon Φ_{BH} and calculate the time evolution of $\phi_{\mathrm{BH}} \coloneqq \Phi_{\mathrm{BH}}/\sqrt{\dot{M}(GM_{\mathrm{BH}}/c^2)^2 c}$, where $\dot{M}$ denotes the rest-mass accretion rate onto the black-hole horizon calculated by $-dM_{>\mathrm{AH}}/dt$ (see the left panel of Fig. 7), and c and G are recovered to clarify the physical units. In our results, $\Phi_{\mathrm{BH}} = (1–4) \times 10^{27}$ G cm^2, and the value of the dimensionless quantity ϕ_{BH} increases with the decrease of $\dot{M}$ in time (see the left panel of Fig. 7). Specifically, irrespective of the initial magnetic-field strength and grid resolution, $\phi_{\mathrm{BH}} \sim 1$ at $t = 100$ ms and ~ 5 at $t = 2$ s for $Q = 4$ and it is slightly smaller for the runs with $Q = 6$. Thus, in our simulation time, ϕ_{BH} is much smaller than 50, which is proposed to be necessary to establish the magnetically arrested disk [106]. In the early stage of its evolution, the accretion disk is a so-called neutrino-dominated accretion disk, for which the mass accretion rate is fairly large and the infall magnetic fluxes are determined by the equipartition condition in the disk, and thus it seems to be difficult to form a disk that satisfies the condition for a magnetically arrested disk. Our results

---

[6]In the magnetohydrodynamics simulation, the flow with low values of ρ/b^2 cannot be accurately computed. Therefore, it is not possible to reproduce the high-Lorentz-factor flow in these simulations.

are quantitatively similar to model BT in Ref. [59], in which the authors considered the evolution of an accretion disk around a spinning black hole with the initial condition of a purely toroidal magnetic field. Our results together with the results in Ref. [59] suggest that, in the absence of an extremely strong poloidal magnetic field on the disk from the beginning, a magnetically arrested disk might not form as a remnant of neutron-star mergers in $t \sim 10$ s. However, we emphasize that (as we have described in this subsection) an intense Poynting flux can be generated even if the condition for a magnetically arrested disk is not satisfied for the case that the rest-mass density along the rotational axis of the black hole becomes sufficiently low in a few hundred ms after the onset of the merger.

Before closing this section, we note the following points. (i) The present simulations were performed imposing equatorial-plane symmetry to save on computational costs. In this setting, asymmetric motion in the turbulent state of the accretion disk is neglected. To fully understand the effects of turbulent motion in the disk and the resulting formation of the magnetosphere, we need to remove such an unphysical symmetry. To clarify the importance of asymmetric motion and also explore the case that the orbital angular momentum and black-hole spin are mis-aligned, we plan to perform a simulation with no plane symmetry as a next step. (ii) The present simulations were started with a poloidal magnetic field confined in the neutron star. The evolution process of the magnetic-field strength is likely to depend on the initial field configuration. In particular, for the case that the field configuration is purely toroidal, the magnetic-field growth rate may be modified significantly in the remnant accretion disk. We also plan to perform simulations with several field configurations in future work.

IV. CONCLUSION

We have reported our new results of general-relativistic neutrino-radiation magnetohydrodynamics simulations for black hole–neutron star mergers. The mass of the black hole and neutron star were chosen to be plausible values ($M_{\mathrm{BH},0} = 5.4$ or $8.1\ M_\odot$ and $M_{\mathrm{NS}} = 1.35\ M_\odot$; cf. Ref. [2]), and we prepared a rapidly spinning black hole with dimensionless spin of 0.75 to consider the case that the neutron star is tidally disrupted in a close orbit. The simulations were performed for ~ 2 s in the longest case to self-consistently explore the dynamical mass ejection, remnant disk evolution, post-merger mass ejection, and collimated Poynting flux generation near the rotational axis of the black hole, which may be related to short-hard gamma-ray bursts.

We found that matter with a mass of 0.04–0.05 $M_\odot$ is ejected dynamically right after tidal disruption of the neutron star on a time scale of $\lesssim 10$ ms, as found in Ref. [41]. Then, an accretion disk with initial rest mass 0.2–0.3 $M_\odot$ forms around the remnant black hole. In the

accretion disk, the magnetohydrodynamics effects such as MRI and winding amplify the magnetic field on a time scale of order 10 ms, and the angular-momentum transport caused by the turbulent motion initially induces mass accretion onto the black hole and disk expansion. In the turbulent process thermal energy is generated, and in the first $\sim$300–500 ms the thermal energy is dissipated by neutrino emission.

However, with the expansion of the accretion disk due to angular-momentum transport and magnetic pressure, the neutrino luminosity eventually drops below $\sim 10^{51.5}$ erg/s. Then, neutrino cooling does not play a role in carrying away thermal energy from the accretion disk, and the thermal energy generated by the turbulent (effectively viscous) process can be fully used for the mass ejection. Then, the post-merger mass ejection sets in. In the present study, the rest mass of the post-merger ejecta was $\sim 0.035\ M_\odot$ and $\sim 0.020\ M_\odot$ for models with $Q = 4$ and 6, respectively. This post-merger mass ejection continues from $t \sim 0.3$ s to ~ 1 s.

Before the post-merger mass ejection sets in, a low rest-mass density funnel with aligned magnetic-field lines forms near the rotational axis of the spinning black hole. This funnel region is magnetically dominant and approximately in a force-free state. In this region, the Blandford-Znajek mechanism extracts the rotational kinetic energy of the rapidly spinning black hole, and a collimated Poynting flux is generated with an opening angle of $\sim 10°$. The estimated maximum isotropic Poynting luminosity is $10^{50} - 10^{51}$ erg/s. Together with the opening angle of the Poynting flux with $\sim 10°$, these numbers are in fair agreement with the typical short-hard gamma-ray bursts [11,12]. The high-Poynting-luminosity stage continues for ~ 1 s and the luminosity subsequently decreases with time due to the expansion of the funnel wall and resulting decrease of the magnetic-flux density. The expansion of the funnel region is caused by the decrease of the rest-mass density and gas pressure around the funnel wall, which takes place due to the post-merger mass ejection. As already mentioned, the post-merger mass ejection sets in after the neutrino luminosity drops and the duration of the post-merger mass ejection is determined by the angular-momentum transport time scale of the accretion disk. Therefore, our present results propose that the typical duration of short-hard gamma-ray bursts may be determined by the evolution time scale of the accretion disk. Specifically, the time scales of neutrino cooling and viscous evolution in the accretion disk (torus) determine the duration of short-hard gamma-ray bursts.

As we have demonstrated in this paper, seconds-long simulations for the merger of neutron-star binaries are necessary to self-consistently explore the entire merger and post-merger processes. This is the case not only for black hole–neutron star binaries, but also for binary neutron stars. We need to focus our effort along this line in the future.

For the case that a black hole forms soon after the merger, we expect that the long-term evolution process (from the merger to the post-merger mass ejection) would be qualitatively the same as that found in this paper, although the quantitative properties of the post-merger ejecta such as the mass and typical electron fraction are likely to depend sensitively on the mass of the remnant black hole and disk. For the case of binary neutron star mergers resulting in a massive neutron star, the post-merger evolution process can be influenced significantly by its presence. If strong global magnetic-field lines anchored by the massive neutron star form soon after the merger, the post-merger mass ejection is likely to be significantly influenced by associated magnetohydrodynamics effects such as the magneto-centrifugal effect [66]. To explore this possibility, we need to consistently follow the evolution of the magnetic-field configuration from the merger through the post-merger stages. Long-term accurate magnetohydrodynamics simulations are particularly desired in the future.

APPENDIX A: EXTENSION OF THE EQUATION OF STATE

Here we describe our method for extending the tabulated nuclear EOS to lower density and temperature. The original DD2 EOS [82] covers a rest-mass density range of $[1.66 \times 10^3 : 1.66 \times 10^{16}]$ g/cm^3 and temperature of $[0.1 : 158]$ MeV, respectively. Hereafter, we will call DD2 the original table. We extend the original EOS to low-density and low-temperature sides using the Timmes EOS [83]. One guiding principle of our extension is to make the internal energy continuous. Otherwise, the primitive recovery procedure in the simulation converges to unphysical values or fails. Here the Timmes EOS contains the effect of not only electrons and positrons with any degeneracy in the nonrelativistic to the highly relativistic regime, but also a nuclei component as an ideal gas and the (photon) radiation component.

While the original table returns thermodynamical quantities as functions of density, temperature, and electron fraction assuming nuclear statistical equilibrium (NSE), the Timmes EOS requires the mean molecular weight of the nuclei as an additional argument. The internal energy of the original EOS table includes the contribution of the nuclear binding energy coming from the fact that the reference mass of a baryon is assumed to be the atomic mass unit (≈ 931 MeV/c^2). However, the Timmes EOS calculates only the thermal part of the internal energy for nuclei, and hence we have to add the contribution of the nuclear binding energy. We first define the contribution of the "nuclear binding energy" $\varepsilon_{\mathrm{nuc}}$ to the specific internal energy by

$$\varepsilon_{\mathrm{nuc}}(\rho, T, Y_{\mathrm{e}}) := \varepsilon^{\mathrm{DD2}}(\rho, T, Y_{\mathrm{e}})$$
$$- \varepsilon^{\mathrm{Timmes}}(\rho, T, Y_{\mathrm{e}}, \mu^{\mathrm{DD2}}(\rho, T, Y_{\mathrm{e}})), \quad \text{(A1)}$$

where $\varepsilon^{\mathrm{DD2}}$ and μ^{DD2} are the specific internal energy and mean molecular weight of the nuclei, respectively, given in the original table, and $\varepsilon^{\mathrm{Timmes}}$ is the specific internal energy derived from the Timmes EOS. We note that $\varepsilon^{\mathrm{DD2}}$ also includes the contribution of the Coulomb energy, and hence $\varepsilon_{\mathrm{nuc}}$ also has its contribution. Using $\varepsilon_{\mathrm{nuc}}$ defined above, we define the specific internal energy in the extended region of (ρ, T) by

$$\varepsilon^{\mathrm{DD2(extended)}}(\rho, T, Y_{\mathrm{e}})$$
$$:= \varepsilon^{\mathrm{Timmes}}(\rho, T, Y_{\mathrm{e}}, \mu^{\mathrm{DD2}}(\rho^*, T^*, Y_{\mathrm{e}}))$$
$$+ \varepsilon_{\mathrm{nuc}}(\rho^*, T^*, Y_{\mathrm{e}}), \quad \text{(A2)}$$

where ρ^* and T^* are defined by

$$\rho^* = \max(\rho, \rho_{\min}^{\mathrm{DD2}}), \quad \text{(A3)}$$

$$T^* = \max(T, T_{\min}^{\mathrm{DD2}}), \quad \text{(A4)}$$

with the minimum density and temperature of the original EOS table $\rho_{\min}^{\mathrm{DD2}} \approx 1.66 \times 10^3$ g/cm^3 and $kT_{\min}^{\mathrm{DD2}} = 0.1$ MeV. The mass fractions of free nucleons and heavy nuclei X_i (i = neutrons, protons, and heavy nuclei) and the average atomic and mass numbers of heavy nuclei $\langle Z \rangle_{\mathrm{heavy}}$ and $\langle A \rangle_{\mathrm{heavy}}$ are defined by

$$X_i^{\mathrm{DD2(extended)}}(\rho, T, Y_{\mathrm{e}}) = X_i^{\mathrm{DD2}}(\rho^*, T^*, Y_{\mathrm{e}}), \quad \text{(A5)}$$

$$\langle Z \rangle_{\mathrm{heavy}}^{\mathrm{DD2(extended)}}(\rho, T, Y_{\mathrm{e}}) = \langle Z \rangle_{\mathrm{heavy}}^{\mathrm{DD2}}(\rho^*, T^*, Y_{\mathrm{e}}), \quad \text{(A6)}$$

$$\langle A \rangle_{\mathrm{heavy}}^{\mathrm{DD2(extended)}}(\rho, T, Y_{\mathrm{e}}) = \langle A \rangle_{\mathrm{heavy}}^{\mathrm{DD2}}(\rho^*, T^*, Y_{\mathrm{e}}). \quad \text{(A7)}$$

Here, "heavy nuclei" refers to nuclei with mass number larger than 4.

This procedure of the extension of the internal energy assumes that the nuclear composition and the contribution of the nuclear binding energy at the low-density or low-temperature region are the same as those at the closest point

of the original table in the ρ-T plane with the same value of Y_{e}. The method guarantees that $\varepsilon^{\mathrm{DD2(extended)}}$ and $\varepsilon^{\mathrm{DD2}}$ are continuously connected at $\rho = \rho_{\min}^{\mathrm{DD2}}$ or $T = T_{\min}^{\mathrm{DD2}}$. Other thermodynamical quantities such as the pressure are obtained using the Timmes EOS as functions of density, temperature, electron fraction, and mean molecular weight of the nuclei. It is a reasonable approximation to assume that nuclei are the ideal gas in a low-density region. Hence, the extension of the pressure can be done in this region without any artificial reprocessing. We note that all thermodynamical quantities are derived using the original table in the parameter region where it is valid.

In this method, the thermodynamical consistency is no longer strictly satisfied in the extended region because we modified the specific internal energy, and the nuclear composition in the NSE is not calculated. However, since the original thermodynamically consistent EOS is used in the high-density ($\geq 1.66 \times 10^3$ g/cm^3) and high-temperature (≥ 0.1 MeV) region where the important magnetohydrodynamics processes proceed, this extension does not affect at least the hydrodynamics in the disk and the launch of post-merger ejecta. In addition, even in the low-density or low-temperature region for which the extended EOS is used, we believe that the effect of the violation of thermodynamical consistency on the hydrodynamics should be minor because we do not artificially modify the pressure in such a region.

With the procedure shown above, we extend the original EOS to the density range $[0.166 : 1.66 \times 10^{16}]$ g/cm^3 and the temperature range $[0.001 : 158]$ MeV. We can set a very-low-density artificial atmosphere with the extended EOS. This is particularly beneficial to investigate the long-term ejecta dynamics from the mergers of neutron star binaries because its dynamics could be affected if a dense artificial atmosphere were present. We set the artificial atmosphere density to 1 g/cm^3 in the far region of the computational domain of our simulation. In this work, the volume of the computational domain is $(0.3\text{–}5) \times 10^{29}$ cm^3, and thus the atmosphere density results in $(0.16\text{–}3) \times 10^{-4} M_\odot$. On the other hand, the mass of the dynamical ejecta, which can first suffer from the effects of the atmosphere, is $\gtrsim 0.04 M_\odot$, which is larger by more than 2 orders of magnitude than the total mass in the atmosphere. Hence, the effects of the artificial atmosphere are expected to be minor.

APPENDIX B: HEATING DUE TO NUCLEAR BURNING

The EOS that we use in this work is derived assuming the NSE for the nuclear composition. Here, we demonstrate how the energy released by nuclear burning is taken into account in such an EOS.

The total energy density e_{tot} in the fluid rest frame including the rest-mass energy is written as

$$e_{\mathrm{tot}} = \sum_i m_i c^2 n_i + e_{\mathrm{int}}, \tag{B1}$$

where m_i and n_i are the mass and number density of the ith nuclear species, and e_{int} is the "pure" internal energy density (i.e., without the rest-mass origin). In our formulation of hydrodynamics and also in constructing the EOS, we define the reference mass of baryons as the atomic unit mass $m_{\mathrm{u}} (\approx 931 \text{ MeV}/c^2)$, and thus the rest-mass density is written as

$$\rho = m_{\mathrm{u}} n_{\mathrm{b}} = m_{\mathrm{u}} \sum_i A_i n_i, \tag{B2}$$

where A_i is the mass number of the ith nuclear species and n_{b} is the baryon number density. Using the definition of ρ, Eq. (B1) can be rewritten as

$$\begin{aligned} e_{\mathrm{tot}} &= \rho c^2 + \left[\sum_i m_i c^2 n_i - \rho c^2 + e_{\mathrm{int}} \right] \\ &= \rho c^2 + \rho \left[\frac{\langle \Delta m \rangle c^2}{m_{\mathrm{u}}} + \varepsilon_{\mathrm{int}} \right], \end{aligned} \tag{B3}$$

where $\varepsilon_{\mathrm{int}} = e_{\mathrm{int}}/\rho$ and

$$\langle \Delta m \rangle = \sum_i (m_i - A_i m_{\mathrm{u}}) \frac{n_i}{n_{\mathrm{b}}} \tag{B4}$$

is the average mass excess per baryon for a given nuclear composition. The quantity inside the brackets of the second term in Eq. (B3), $e_{\mathrm{tot}}/\rho - c^2$, is the "specific internal energy" ε in our formulation.

Then, we consider the variation of only the nuclear composition. That is, we consider the change of $\langle \Delta m \rangle$ when keeping the total energy density e_{tot} fixed. From Eq. (B3), we have

$$0 = d e_{\mathrm{tot}}|_{\mathrm{comp}} = \rho \left[\frac{c^2}{m_{\mathrm{u}}} d \langle \Delta m \rangle + d\varepsilon_{\mathrm{int}}|_{\mathrm{comp}} \right], \tag{B5}$$

where $dX|_{\mathrm{comp}}$ is the variation of the quantity X associated only with the change in the composition. We note that $\rho = m_{\mathrm{u}} n_{\mathrm{b}}$ does not change by the modification of the nuclear composition. As a result,

$$d\varepsilon_{\mathrm{int}}|_{\mathrm{comp}} = -\frac{c^2}{m_{\mathrm{u}}} d\langle \Delta m \rangle. \tag{B6}$$

Equation (B6) clearly shows that the nuclear burning, which results in the modification of the nuclear composition, simply changes the internal energy, and thus this is the net specific heating by the nuclear burning. For example, $\langle \Delta m \rangle \approx 7.4 \text{ MeV}/c^2$ for the production of iron from matter composed of half free protons and half free neutrons, and $\langle \Delta m \rangle \approx 1.4 \text{ MeV}/c^2$ from only alpha particles. Thus, if

protons and neutrons completely recombine into alpha particles in the matter with $Y_e = 0.5$, 6.0 MeV per baryon is released to increase ε_{int}.

It is important to note that the heating by the nuclear burning is automatically incorporated without adding any source term in the equations of hydrodynamics if the change in the average mass excess by the nuclear burning is taken into account. The net specific heating rate by the nuclear reaction is written as

$$\left.\frac{d\varepsilon_{int}}{dt}\right|_{comp} = -\frac{c^2}{m_u}\frac{d\langle\Delta m\rangle}{dt}. \quad\text{(B7)}$$

The time derivative of $\langle\Delta m\rangle$ is in general written as

$$\frac{d\langle\Delta m\rangle}{dt} = \sum_i (m_i - A_i m_u)\frac{1}{n_b}\frac{dn_i}{dt}, \quad\text{(B8)}$$

where dn_i/dt is the time derivative of the number density of the ith species (this method was employed in, e.g., Ref. [107]). On the other hand, in the NSE, $\langle\Delta m\rangle$ is a function of the baryon number density (or ρ), temperature, and electron fraction, and thus the net heating rate by nuclear burning can be expressed as

$$\frac{d\langle\Delta m\rangle}{dt} = \frac{\partial\langle\Delta m\rangle}{\partial\rho}\frac{d\rho}{dt} + \frac{\partial\langle\Delta m\rangle}{\partial T}\frac{dT}{dt} + \frac{\partial\langle\Delta m\rangle}{\partial Y_e}\frac{dY_e}{dt}. \quad\text{(B9)}$$

APPENDIX C: ON THE RESOLUTION OF MRI

Figure 16 shows snapshots of the MRI quality factor defined by $\lambda_{zMRI}/\Delta x$ in the x-z plane for model Q4B5L. Here, λ_{zMRI} is the wavelength of the fastest growing mode of the axisymmetric MRI, which is defined by

$$\lambda_{zMRI} = \frac{b_z}{\sqrt{4\pi\rho h + b^\mu b_\mu}}\frac{2\pi}{\Omega}, \quad\text{(C1)}$$

where Ω denotes the local angular velocity and the z direction is the direction of the rotation axis. The similar feature is also found for other time slices. Figure 16 shows that the fastest growing mode is covered by more than 20 grid points in a large portion of the disk even for the low-resolution run ($\lambda_{zMRI} \sim 10$ km in the inner region of the disk), and thus we consider that the fastest growing mode of the MRI is resolved with a reasonable accuracy in the present work.

APPENDIX D: EVIDENCE FOR THE BLANDFORD-ZNAJEK MECHANISM

Figure 17 shows snapshots of an outgoing Poynting flux per steradian near the apparent horizon defined by $-T^{(EM)r}_{\ \ t}\sqrt{-g}/\sin\theta$. Along the poloidal magnetic-field line, the outgoing Poynting flux is distributed from the
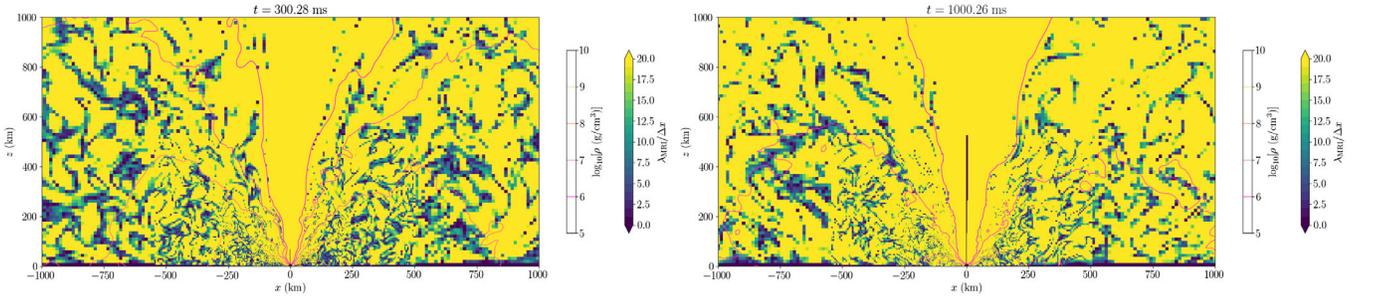

FIG. 16. Snapshots of the MRI quality factor together with the rest-mass density (contour) in the x-z plane at $t \approx 300$ and 1000 ms for model Q4B5L.
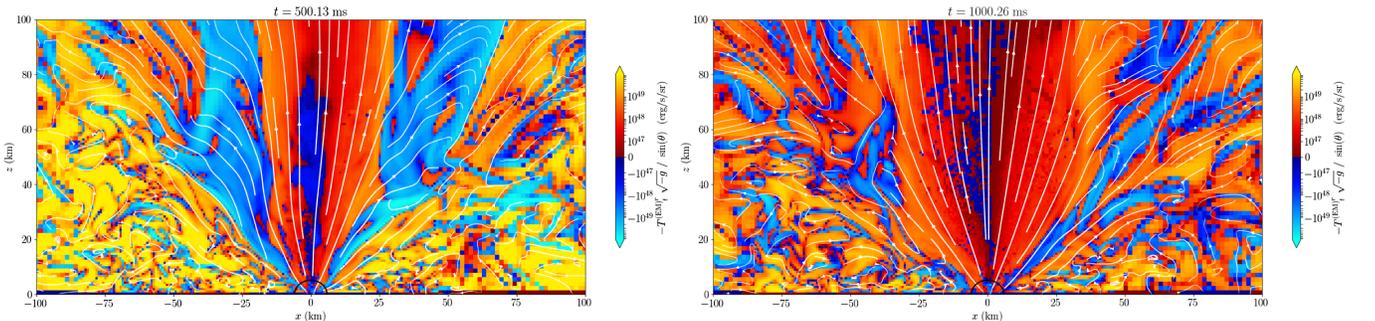

FIG. 17. Snapshots of the outgoing Poynting flux per steradian together with poloidal magnetic-field lines (white curves) near the apparent horizon in the x-z plane at $t \approx 500$ and 1000 ms for model Q4B5L. The apparent horizon is shown with the black circle.

apparent horizon to the magnetosphere around the rotational axis of the black hole. This indicates that energy is extracted from the black hole through the magnetic field, and thus we can interpret that the Blandford-Znajek mechanism is in operation. In addition, we find that the total Poynting luminosity on the apparent horizon is $\sim 10^{49}$ erg/s. This value is consistent with the luminosity expected from the formula for the Blandford-Znajek mechanism [95] for the resultant values of the magnetic-field strength, black-hole mass, and spin.

[1] B. P. Abbott *et al.* (LIGO Scientific and Virgo Collaborations), Phys. Rev. Lett. **116**, 061102 (2016).

[2] R. Abbott *et al.* (LIGO Scientific and Virgo Collaborations), Phys. Rev. X **11**, 021053 (2021).

[3] R. Abbott *et al.*, arXiv:2111.03606.

[4] B. P. Abbott *et al.* (LIGO Scientific and Virgo Collaborations), Phys. Rev. Lett. **119**, 161101 (2017).

[5] B. P. Abbott *et al.*, Astrophys. J. **848**, L12 (2017).

[6] B. P. Abbott *et al.*, Astrophys. J. **848**, L13 (2017).

[7] R. Abbott *et al.*, Astrophys. J. **915**, L5 (2021).

[8] M. Shibata and K. Taniguchi, Living Rev. Relativity **14**, 6 (2011).

[9] K. Kyutoku, M. Shibata, and K. Taniguchi, Living Rev. Relativity **24**, 5 (2021).

[10] D. Eichler, M. Livio, T. Piran, and D. N. Schramm, Nature (London) **340**, 126 (1989).

[11] E. Nakar, Phys. Rep. **442**, 166 (2007).

[12] E. Berger, Annu. Rev. Astron. Astrophys. **52**, 43 (2014).

[13] J. M. Lattimer and D. N. Schramm, Astrophys. J. **192**, L145 (1974).

[14] L.-X. Li and B. Paczyński, Astrophys. J. **507**, L59 (1998).

[15] B. D. Metzger, G. Martínez-Pinedo, S. Darbha, E. Quataert, A. Arcones, D. Kasen, R. Thomas, P. Nugent, I. V. Panov, and N. T. Zinner, Mon. Not. R. Astron. Soc. **406**, 2650 (2010).

[16] M. Shibata and K. Uryū, Phys. Rev. D **74**, 121503 (2006).

[17] M. Shibata and K. Uryū, Classical Quantum Gravity **24**, S125 (2007).

[18] M. Shibata and K. Taniguchi, Phys. Rev. D **77**, 084015 (2008).

[19] Z. B. Etienne, J. A. Faber, Y. T. Liu, S. L. Shapiro, K. Taniguchi, and T. W. Baumgarte, Phys. Rev. D **77**, 084002 (2008).

[20] M. D. Duez, F. Foucart, L. E. Kidder, H. P. Pfeiffer, M. A. Scheel, and S. A. Teukolsky, Phys. Rev. D **78**, 104015 (2008).

[21] M. Shibata, K. Kyutoku, T. Yamamoto, and K. Taniguchi, Phys. Rev. D **79**, 044030 (2009).

[22] Z. B. Etienne, Y. T. Liu, S. L. Shapiro, and T. W. Baumgarte, Phys. Rev. D **79**, 044024 (2009).

[23] S. Chawla, M. Anderson, M. Besselman, L. Lehner, S. L. Liebling, P. M. Motl, and D. Neilsen, Phys. Rev. Lett. **105**, 111101 (2010).

[24] M. D. Duez, F. Foucart, L. E. Kidder, C. D. Ott, and S. A. Teukolsky, Classical Quantum Gravity **27**, 114106 (2010).

[25] K. Kyutoku, M. Shibata, and K. Taniguchi, Phys. Rev. D **82**, 044049 (2010).

[26] K. Kyutoku, H. Okawa, M. Shibata, and K. Taniguchi, Phys. Rev. D **84**, 064018 (2011).

[27] F. Foucart, M. D. Duez, L. E. Kidder, and S. A. Teukolsky, Phys. Rev. D **83**, 024005 (2011).

[28] F. Foucart, M. D. Duez, L. E. Kidder, M. A. Scheel, B. Szilagyi, and S. A. Teukolsky, Phys. Rev. D **85**, 044015 (2012).

[29] Z. B. Etienne, Y. T. Liu, V. Paschalidis, and S. L. Shapiro, Phys. Rev. D **85**, 064029 (2012).

[30] Z. B. Etienne, V. Paschalidis, and S. L. Shapiro, Phys. Rev. D **86**, 084026 (2012).

[31] K. Kyutoku, K. Ioka, and M. Shibata, Phys. Rev. D **88**, 041503 (2013).

[32] K. Kyutoku, K. Ioka, H. Okawa, M. Shibata, and K. Taniguchi, Phys. Rev. D **92**, 044028 (2015).

[33] F. Foucart, M. B. Deaton, M. D. Duez, L. E. Kidder, I. MacDonald, C. D. Ott, H. P. Pfeiffer, M. A. Scheel, B. Szilagyi, and S. A. Teukolsky, Phys. Rev. D **87**, 084006 (2013).

[34] G. Lovelace, M. D. Duez, F. Foucart, L. E. Kidder, H. P. Pfeiffer, M. A. Scheel, and B. Szilágyi, Classical Quantum Gravity **30**, 135004 (2013).

[35] M. B. Deaton, M. D. Duez, F. Foucart, E. O'Connor, C. D. Ott, L. E. Kidder, C. D. Muhlberger, M. A. Scheel, and B. Szilagyi, Astrophys. J. **776**, 47 (2013).

[36] F. Foucart, M. B. Deaton, M. D. Duez, E. O'Connor, C. D. Ott, R. Haas, L. E. Kidder, H. P. Pfeiffer, M. A. Scheel, and B. Szilagyi, Phys. Rev. D **90**, 024026 (2014).

[37] V. Paschalidis, M. Ruiz, and S. L. Shapiro, Astrophys. J. **806**, L14 (2015).

[38] K. Kawaguchi, K. Kyutoku, H. Nakano, H. Okawa, M. Shibata, and K. Taniguchi, Phys. Rev. D **92**, 024014 (2015).

[39] K. Kiuchi, Y. Sekiguchi, K. Kyutoku, M. Shibata, K. Taniguchi, and T. Wada, Phys. Rev. D **92**, 064034 (2015).

[40] F. Foucart, D. Desai, W. Brege, M. D. Duez, D. Kasen, D. A. Hemberger, L. E. Kidder, H. P. Pfeiffer, and M. A. Scheel, Classical Quantum Gravity **34**, 044002 (2017).

[41] K. Kyutoku, K. Kiuchi, Y. Sekiguchi, M. Shibata, and K. Taniguchi, Phys. Rev. D **97**, 023009 (2018).

[42] W. Brege, M. D. Duez, F. Foucart, M. B. Deaton, J. Caro, D. A. Hemberger, L. E. Kidder, E. O'Connor, H. P. Pfeiffer, and M. A. Scheel, Phys. Rev. D **98**, 063009 (2018).

[43] M. Ruiz, S. L. Shapiro, and A. Tsokaros, Phys. Rev. D **98**, 123017 (2018).

[44] F. Foucart, M. D. Duez, T. Hinderer, J. Caro, A. R. Williamson, M. Boyle, A. Buonanno, R. Haas,

D. A. Hemberger, L. E. Kidder, H. P. Pfeiffer, and M. A. Scheel, Phys. Rev. D **99**, 044008 (2019).

[45] F. Foucart, M. D. Duez, L. E. Kidder, S. M. Nissanke, H. P. Pfeiffer, and M. A. Scheel, Phys. Rev. D **99**, 103025 (2019).

[46] T. Hinderer, S. Nissanke, F. Foucart, K. Hotokezaka, T. Vincent, M. Kasliwal, P. Schmidt, A. R. Williamson, D. A. Nichols, M. D. Duez, L. E. Kidder, H. P. Pfeiffer, and M. A. Scheel, Phys. Rev. D **100**, 063021 (2019).

[47] K. Hayashi, K. Kawaguchi, K. Kiuchi, K. Kyutoku, and M. Shibata, Phys. Rev. D **103**, 043007 (2021).

[48] F. Foucart, A. Chernoglazov, M. Boyle, T. Hinderer, M. Miller, J. Moxon, M. A. Scheel, N. Deppe, M. D. Duez, F. Hébert, L. E. Kidder, W. Throwe, and H. P. Pfeiffer, Phys. Rev. D **103**, 064007 (2021).

[49] S. V. Chaurasia, T. Dietrich, and S. Rosswog, Phys. Rev. D **104**, 084010 (2021).

[50] E. R. Most, L. J. Papenfort, S. D. Tootle, and L. Rezzolla, Mon. Not. R. Astron. Soc. **506**, 3511 (2021).

[51] R. Fernández and B. D. Metzger, Mon. Not. R. Astron. Soc. **435**, 502 (2013).

[52] B. D. Metzger and R. Fernández, Mon. Not. R. Astron. Soc. **441**, 3444 (2014).

[53] O. Just, A. Bauswein, R. A. Pulpillo, S. Goriely, and H.-T. Janka, Mon. Not. R. Astron. Soc. **448**, 541 (2015).

[54] R. Fernández, E. Quataert, J. Schwab, D. Kasen, and S. Rosswog, Mon. Not. R. Astron. Soc. **449**, 390 (2015).

[55] R. Fernández, F. Foucart, D. Kasen, J. Lippuner, D. Desai, and L. F. Roberts, Classical Quantum Gravity **34**, 154001 (2017).

[56] D. M. Siegel and B. D. Metzger, Astrophys. J. **858**, 52 (2018).

[57] R. Fernández, A. Tchekhovskoy, E. Quataert, F. Foucart, and D. Kasen, Mon. Not. R. Astron. Soc. **482**, 3373 (2019).

[58] A. Janiuk, Astrophys. J. **882**, 163 (2019).

[59] I. M. Christie, A. Lalakos, A. Tchekhovskoy, R. Fernández, F. Foucart, E. Quataert, and D. Kasen, Mon. Not. R. Astron. Soc. **490**, 4811 (2019).

[60] J. M. Miller, B. R. Ryan, J. C. Dolence, A. Burrows, C. J. Fontes, C. L. Fryer, O. Korobkin, J. Lippuner, M. R. Mumpower, and R. T. Wollaeger, Phys. Rev. D **100**, 023008 (2019).

[61] S. Fujibayashi, M. Shibata, S. Wanajo, K. Kiuchi, K. Kyutoku, and Y. Sekiguchi, Phys. Rev. D **101**, 083029 (2020).

[62] S. Fujibayashi, M. Shibata, S. Wanajo, K. Kiuchi, K. Kyutoku, and Y. Sekiguchi, Phys. Rev. D **102**, 123014 (2020).

[63] X. Li and D. M. Siegel, Phys. Rev. Lett. **126**, 251101 (2021).

[64] R. Fernández, F. Foucart, and J. Lippuner, Mon. Not. R. Astron. Soc. **497**, 3221 (2020).

[65] O. Just, S. Goriely, H. T. Janka, S. Nagataki, and A. Bauswein, Mon. Not. R. Astron. Soc. **509**, 1377 (2021).

[66] M. Shibata, S. Fujibayashi, and Y. Sekiguchi, Phys. Rev. D **104**, 063026 (2021).

[67] M. Shibata and T. Nakamura, Phys. Rev. D **52**, 5428 (1995).

[68] T. W. Baumgarte and S. L. Shapiro, Phys. Rev. D **59**, 024007 (1998).

[69] M. Campanelli, C. O. Lousto, P. Marronetti, and Y. Zlochower, Phys. Rev. Lett. **96**, 111101 (2006).

[70] J. G. Baker, J. Centrella, D.-I. Choi, M. Koppitz, and J. van Meter, Phys. Rev. Lett. **96**, 111102 (2006).

[71] P. Marronetti, W. Tichy, B. Brügmann, J. González, and U. Sperhake, Phys. Rev. D **77**, 064010 (2008).

[72] D. Hilditch, S. Bernuzzi, M. Thierfelder, Z. Cao, W. Tichy, and B. Brügmann, Phys. Rev. D **88**, 084057 (2013).

[73] M. Shibata and Y. Sekiguchi, Phys. Rev. D **72**, 044014 (2005).

[74] M. Shibata, Y. Sekiguchi, and R. Takahashi, Prog. Theor. Phys. **118**, 257 (2007).

[75] K. Kiuchi, K. Kyutoku, and M. Shibata, Phys. Rev. D **86**, 064008 (2012).

[76] C. R. Evans and J. F. Hawley, Astrophys. J. **332**, 659 (1988).

[77] D. S. Balsara, J. Comput. Phys. **228**, 5040 (2009).

[78] Y. Sekiguchi, K. Kiuchi, K. Kyutoku, and M. Shibata, Prog. Theor. Exp. Phys. **2012**, 01A304 (2012).

[79] K. S. Thorne, Mon. Not. R. Astron. Soc. **194**, 439 (1981).

[80] M. Shibata, K. Kiuchi, Y. Sekiguchi, and Y. Suwa, Prog. Theor. Phys. **125**, 1255 (2011).

[81] S. Fujibayashi, S. Wanajo, K. Kiuchi, K. Kyutoku, Y. Sekiguchi, and M. Shibata, Astrophys. J. **901**, 122 (2020).

[82] S. Banik, M. Hempel, and D. Bandyopadhyay, Astrophys. J. **214**, 22 (2014).

[83] F. X. Timmes and F. D. Swesty, Astrophys. J. **126**, 501 (2000).

[84] M. C. Miller et al., Astrophys. J. Lett. **887**, L24 (2019).

[85] S. A. Balbus and J. F. Hawley, Astrophys. J. **376**, 214 (1991).

[86] S. A. Balbus and J. F. Hawley, Rev. Mod. Phys. **70**, 1 (1998).

[87] Y. Masada and T. Sano, Astrophys. J. **689**, 1234 (2008).

[88] J. Guilet, A. Bauswein, O. Just, and H.-T. Janka, Mon. Not. R. Astron. Soc. **471**, 1879 (2017).

[89] https://www2.yukawa.kyoto-u.ac.jp/~kota.hayashi/Q4B5L-2000a.mp4.

[90] A. Brandenburg and K. Subramanian, Phys. Rep. **417**, 1 (2005).

[91] R. D. Blandford and D. G. Payne, Mon. Not. R. Astron. Soc. **199**, 883 (1982).

[92] G. M. Fuller, W. A. Fowler, and M. J. Newman, Astrophys. J. **293**, 1 (1985).

[93] B. D. Metzger, A. L. Piro, and E. Quataert, Mon. Not. R. Astron. Soc. **390**, 781 (2008).

[94] M. Liska, A. Tchekhovskoy, and E. Quataert, Mon. Not. R. Astron. Soc. **494**, 3656 (2020).

[95] R. D. Blandford and R. L. Znajek, Mon. Not. R. Astron. Soc. **179**, 433 (1977).

[96] M. Shibata, Y. T. Liu, S. L. Shapiro, and B. C. Stephens, Phys. Rev. D **74**, 104026 (2006).

[97] J. M. Bardeen, W. H. Press, and S. A. Teukolsky, Astrophys. J. **178**, 347 (1972).

[98] S. De and D. M. Siegel, Astrophys. J. **921**, 94 (2021).

[99] A. M. Beloborodov, Astrophys. J. **588**, 931 (2003).

[100] K. Hotokezaka, K. Kiuchi, K. Kyutoku, H. Okawa, Y. Sekiguchi, M. Shibata, and K. Taniguchi, Phys. Rev. D **87,** 024001 (2013).

[101] S. Wanajo, Y. Sekiguchi, N. Nishimura, K. Kiuchi, K. Kyutoku, and M. Shibata, Astrophys. J. **789,** L39 (2014).

[102] K. Kawaguchi, M. Shibata, and M. Tanaka, Astrophys. J. **889,** 171 (2020).

[103] https://www2.yukawa.kyoto-u.ac.jp/~kota.hayashi/Q4B5L-3D.mp4.

[104] https://www2.yukawa.kyoto-u.ac.jp/~kota.hayashi/Q4B5L-mf.mp4.

[105] https://www2.yukawa.kyoto-u.ac.jp/~kota.hayashi/Q4B5L-f3D.mp4.

[106] A. Tchekhovskoy, R. Narayan, and J. C. McKinney, Mon. Not. R. Astron. Soc. **418,** L79 (2011).

[107] H. Uchida, M. Shibata, T. Yoshida, Y. Sekiguchi, and H. Umeda, Phys. Rev. D **96,** 083016 (2017).